The Numerical Simulation and Performance Assessment of Rim-Driven Turbine

Akezhan Zholdybayev, BEng

Submitted in fulfillment of the requirements
for the degree of Master of Science
in Mechanical & Aerospace Engineering

School of Engineering and Digital Sciences
Department of Mechanical & Aerospace Engineering
Nazarbayev University

53 Kabanbay Batyr Avenue,
Astana, Kazakhstan, 010000

Supervisor: Associate Professor Basman Elhadidi
Co-supervisor: Associate Professor Luis Rojas-Solórzano

April 2023

DECLARATION

I hereby, declare that this manuscript, entitled "*The numerical simulation and analysis of the performance of Rim-driven Turbine*", is the result of my own work except for quotations and citations, which have been duly acknowledged.

I also declare that, to the best of my knowledge and belief, it has not been previously or concurrently submitted, in whole or in part, for any other degree or diploma at Nazarbayev University or any other national or international institution.

Name: Akezhan Zholdybayev
Date: 07.04.2023

Abstract

Global warming and rising environmental pollution have pushed scientists and engineers to develop new energy-harnessing methods. One promising solution is converting the kinetic and potential energy contained in water into electricity using a hydraulic turbine.

This thesis research will use CFD analysis to study the effectiveness of converting kinetic water energy into electric energy in a pipe for a Rim-driven Turbine (RDT), which offers the advantage of being easily installed in drainage and water running systems.

Previous research in the area of RDT has demonstrated that the field contains a lot of research gaps that need to be addressed, such as a lack of material on parameters that affect performance, including cavitation, geometry, and simulations comprising different environmental conditions. Therefore, the numerical simulation of an RDT is presented focused on assessing its essential parameters, including power curves demonstrating the effectively generated energy ratio.

A configuration of several RDT in series in a pipe was considered to reduce blade loading. The results show that installing RDT in series reduces the pressure drop on each turbine while nearly doubling the power output for the same pressure head in the pipe.

Acknowledgments

First and foremost, my sincere thanks go to my parents, whose wisdom and support assisted me during the most challenging times.

In addition, I would like to express my gratitude towards my supervisor, Professor Basman Elhadidi, who allowed me to research the field and guided me throughout my MSc thesis. His recommendations allowed me to develop the necessary skills to conduct the following research.

Last but not least, I am thankful to Professor Luis Rojas-Solórzano, whose comments and recommendations helped me to address the problem from a new perspective.

Table of Contents

List of Abbreviations & Symbols (Example)

CFD	Computational Fluid Dynamics
P	Static pressure
T	Temperature
S_m	Mass added from the source
C_p	Power coefficient
V_0	Free-stream velocity
$\|V\|$	Velocity magnitude
MRF	Moving Reference Frame
TSR	Tip-speed-ratio
RDT	Rim-driven turbine
S	Blade swept area
AFM	Atomic force microscope
PIV	Particle Image Velocimetry
PO	Power output
ω	Angular velocity

List of Tables

List of Figures

Chapter 1 – Introduction

1.1. Background

The rising global temperature pushes countries to seek alternative sources due to increasing carbon dioxide levels and other greenhouse gases. One of the promising solutions is green energy sources that produce a minimum environmental footprint. Currently, they make up a third of the world's energy supply, which shows their importance in the current energy market (Ritchie, 2022). They comprise solar, hydro, wind, thermal, and biomass energy. In the case of Kazakhstan, most of the energy produced comes from coal, oil, and gas, which encompass 54.74 %, 22.14%, and 19.13% of the energy supply, correspondingly.

In terms of hydro-energy potential, the country possesses mountainous terrain with runoff water in the Altai Mountains and Dzungar Alatau Mountains with 0.4-1.8 km/m^2 river density. However, it is possible to harness hydro energy from other means, such as sewage water systems in every city. It requires unique design concepts, and one of them is the Rim-driven Turbine (RDT). The absence of a central hub provides several advantages over regular turbines: reduced flow resistance, disturbance, and noise generation (Song, 2021). Moreover, it can be integrated into water pipes with flowing water in runoff mountain waters and sewage systems.

An RDT consists of stator, rotor, duct, and blades, as demonstrated in Fig.1. The first concept of RDT was introduced by Ludwig Kort (Kort, 1940), a German scientist investigating methods to reduce cavitation. The idea led to the creation of ducted propellers, which offered higher thrusts. Later, similar designs were patented by other scientists and engineers (Pierro, 1973; Edwards et al., 1988; Taylor et al., 1989). Yet, the technology remained unpopular until the development of DC motors (Xinping, 2017), which led to variations of the overall RDT technology, including the turbine.

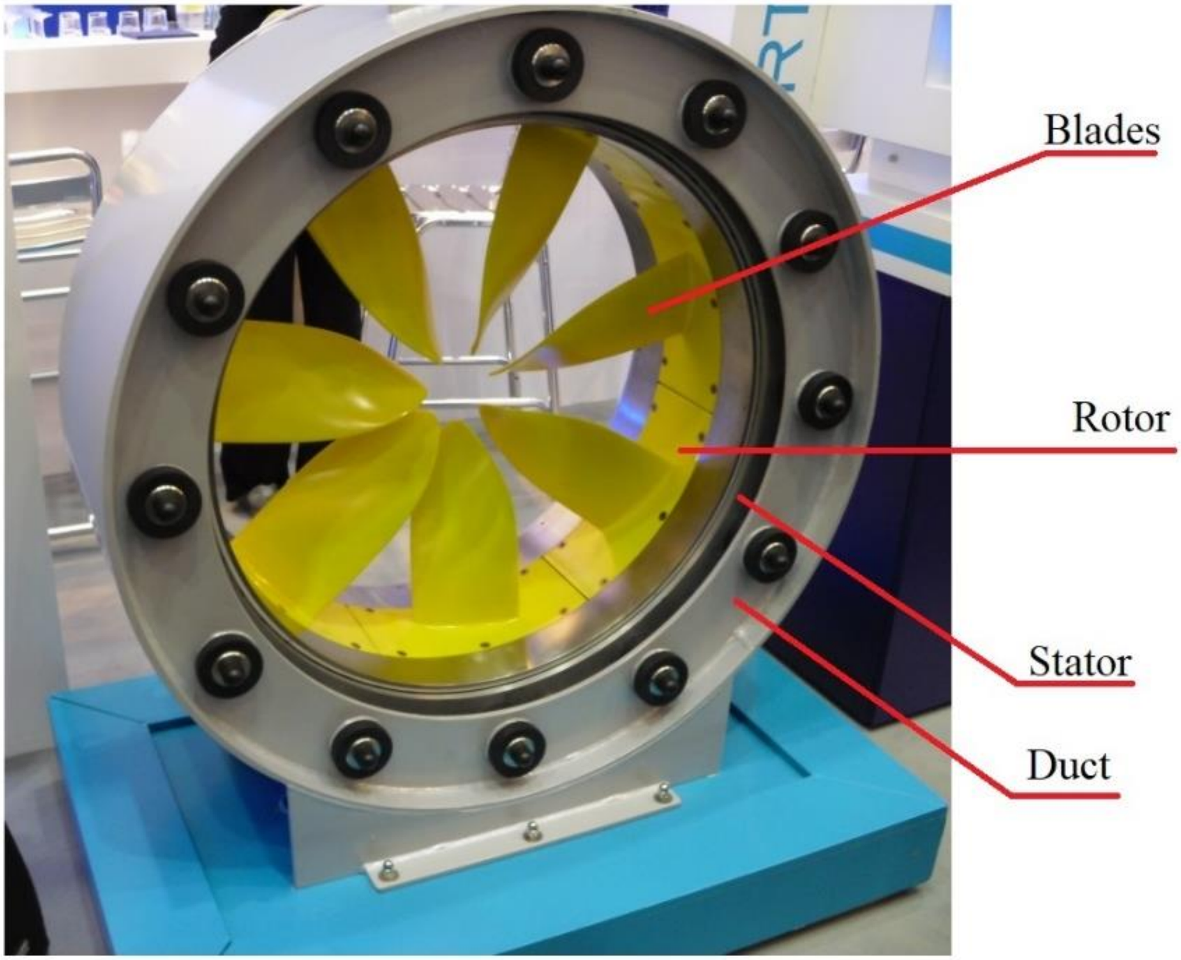

Figure 1. Structure of a Rim-driven turbine (RDT) (Hochhaus, 2010).

The working principle of RDT turbines is similar to traditional turbines with a central hub. The flow of water through the blades moves the blades converting the kinetic energy of the fluid to electric power. The design provides increased flexibility during installations, less vibration, noise, and a reduced rate of failures.

1.2. Literature Review

1.2.1 Investigation of Application Areas

The novelty of this technology brings challenges for researchers interested in developing the field, with a lack of experimental data and research material being the most critical problems. The recent research is devoted to the development or design of magnetic parts of the turbine (Gieras, 2008; Kim. 2013; Djebarri, 2012; Djebarri, 2015) or application of the technology as a thruster, not as a generator (Xinping, 2017; Kim, 2020).

Observing the literature chronologically, we can see that some works on electromagnetic aspects of RDT turbines were initiated for marine-current turbines (Gieras, 2008; Djebarri, 2012; Kim, 2013; Xu, 2017). Further, a similar approach was conducted for tidal turbines (Djebarri, 2014; Djebarri, 2015), demonstrating how scientists were trying to extend the application of shaftless ducted turbines in different scenarios.

The analysis of the RDT turbine application areas has demonstrated that they are primarily utilized as thrusters, marine-current turbines, and tidal turbines, revealing a restricted scope of their potential applications. Thus, assessing the technology in other scenarios is necessary to address the research gap in existing and new application areas.

1.2.2 Numerical & Experimental Studies of RDT

Song and Yang (2021) work on "shaftless RDT" is an excellent example where the influence of shaft diameter on hydrodynamic performance is present. As a result, they have found a positive relationship between the shaft diameter size with power output and thrust. Further, they initiated a similar work (Song, 2022) focused on numerical analysis of the performance of RDTs in real-case scenarios. First, they developed a numerical model in ANSYS Fluent with "DT08XX" blades for the rotor. Second, they specified the computational domain where the data for boundary conditions were taken from the "Chinese National Agency" for Zhaitang Islands in the East China Sea. Lastly, the validation was conducted by comparing power coefficients (Cp) for different tip-speed ratios (TSR) with a similar experimental study on diffuser-augmented turbines (Song, 2018).

Jiang et al. (2022) developed an analytical model to study the generator's effectiveness with the assessment of the effects of blades on hydrodynamic performance. The results indicate that the smaller groove depths have a low impact on power output. Yet, their work lacked experimental data on values on different ranges of blades rpm, which is crucial in deriving the whole image of the turbine's performance. Additionally, the authors propose the rough design of a counter-rotating thruster with Ka 4-70 duct propeller and focus on several goals: establishing three geometric models, studying the flow distribution, the fluid gap friction and flow channel, and deriving the relationship between the effects of gap fluid and performance. But there was a lack of comparison between numerical and experimental data. While the experiments on thrusts seem out of scope, it contains essential data on a counter rotation of the blades. As a result, Jian et al.'s work could be extended to the numerical analysis of RDT turbines where counter rotation of the blades is assessed.

Several experimental studies used various tests and conditions, such as the work by Santoso et al. (2017). They modified the thickness distribution of the Ka-70 hydro-turbine in the Open Water Test and derived the relationship between rpm and power for motor loads. Yet, the work lacks test results for a different pitch. Nevertheless, the outcome might be helpful in its data on rpm, loads, and thickness distribution for similar studies on RDT turbines. Abbas et al. (2017) conducted similar work on Kaplan hydro-turbines at low heads. Likewise, the authors optimized various design parameters for maximum power output.

Interestingly, only a single work based on the direct effect of cavitation on RDT performance was present in the literature (Zhu, 2021), even though such an effect might drastically impact overall performance. To put it briefly, the authors took a reversible pump-turbine and tested it in both numerical and experimental analysis. As a result, they have derived the cavitation pattern ranging from no cavitation to critical one, which causes the fluctuations of axial forces.

1.2.3 Studies on Blades Cavitation

Cavitation is a severe issue that affects the performance of hydro-machinery by causing erosion of their blades. Thus, researchers tried to address it with different approaches. For instance, Patella et al. (2013) proposed a new method that uses an oligocyclic fatigue approach and measured material damage with EdF-R&D. Then, they calculated the mass loss rate for different cases with validation and demonstrated that the erosion rate and the pitting rate have a linear relationship. However, the authors state that the work requires more experimental data for the fatigue energy criterion. Blade erosion has different types depending on the bubbles' behavior. Leading edge cavitation is one of the most severe types affecting performance. Therefore, Escaler et al. (2004) tried to detect it via numerical simulation, analyzing vibrations, noise emissions, and hydrodynamic pressures on Kaplan, Francis, and Pump turbines. The results show that cavitating vortex core occurs at 50% of the maximum load for pump turbines. In contrast, erosive inlet cavitation is present in their Francis turbine at a load of 30 MW. Moreover, their study showed that leading-edge cavitation was less likely to occur at Kaplan turbines than at Francis turbines. The review of current research on cavitation and performance has demonstrated that researchers chose pump, marine-current, Kaplan, and tidal turbines as test subjects for these studies. For example, Hötzl et al. (2017) designed an axial tidal turbine with the help of CFD.

An experimental work addressing cavitation in tidal turbines was done by Mineshima et al. (2019). To be precise, the turbine's performance was increased by choosing the optimal blade design free of leading-edge cavitation. In contrast to the blade design, the authors studied hydrophilic and hydrophobic polymers as coatings to prevent erosion inception of the blade. The measurements on atomic force microscope (AFM) demonstrated that hydrophilic coating has better results in preventing blade erosion. Interestingly, Fialova et al. (2016) did another work on hydrophilic coating, where a Francis turbine was tested. The measurements of velocity profiles for the Francis turbine were taken with Particle Image Velocimetry (PIV), and the results demonstrated a 20% reduction in performance loss. However, the performance losses also might be caused by friction of the disks, so it is advised to use a different type of coatings to address performance reduction associated with the action of turbulent eddies.

1.2.4 Summary

In the literature review, it was identified that there was a lack of research material that addresses the hydrodynamic performance of RDT. In contrast, most research found is in the context of thrusters and as a part of the electromagnetic element. At the same time, four previous research were directly related to our CFD study of the RDT turbines. However, only the work by Song et al. (2018, 2021) was based on CFD analysis of the RDT performance, while others (e.g., Djebarri et al., 2012, 2015; Jiang, 2022) addressed electromagnetic parts and gap fluids, which are out of scope in this thesis research. Expanding the search area by including other technologies on hydro performance demonstrated that a large amount of work was focused on marine-current, pump, Kaplan, and Francis turbines, especially in the case of cavitation, which severely affects the performance of the blade. It was found that leading edge and tip-vortex cavitation is the most common type in such technologies. It was addressed by conducting an experimental study using different measurement tools such as PIV and AFM. However, it was observed that these works had not addressed high inflow velocities with large Re numbers where high-pressure gradients on blades are present, which might be related to the limitations of the experimental setups. Therefore, it was decided to conduct a numerical analysis that would assess the hydrodynamic performance of the RDT turbines, where high Re numbers would be taken into consideration.

1.3. Motivation

As it was mentioned before, similar studies have not considered the performance of RDTs in a pipe with water flow. The formulation allows generalizing the problem into different conditions where the turbine would be hypothetically installed. These situations include but are not limited to water flow in a sewer system, downhill flow, and any systems with the flow in a pipe. Thus, we can adjust the experiment for cases and generate relevant data. However, at the initial stage, we will only consider the water flow in a given direction for specified boundary conditions.

1.4. Pressure Loads and Power Output

Hydro-turbines blades are subject to significant pressure loads, which can cause substantial damage and a reduced operational lifespan. These loads induce erosion, fatigue, and surface corrosion, forming cracks and eventual failure. It is necessary to decrease the pressure loads on the blades to mitigate wear and tear and prolong the system's lifespan while reducing maintenance and repair costs.

In this context, we propose a hypothesis regarding the arrangement-in-series of RDT. This hypothesis suggests that a sudden pressure drop on multiple turbines connected in series within a pipe can lead to lower pressure loads on the blades' surfaces than for a single hydro-turbine. Additionally, it is crucial to determine whether doubling the number of turbines is more cost-effective and efficient than doubling the number of blades. Therefore, we will evaluate an additional case involving a hydro-turbine with twice the number of blades and compare it to two hydro-turbines connected in series. As demonstrated in Fig. 2, three cases are studied to confirm that the series connection reduces pressure drops on the blades' surface and provides a cost-effective solution for the problem.

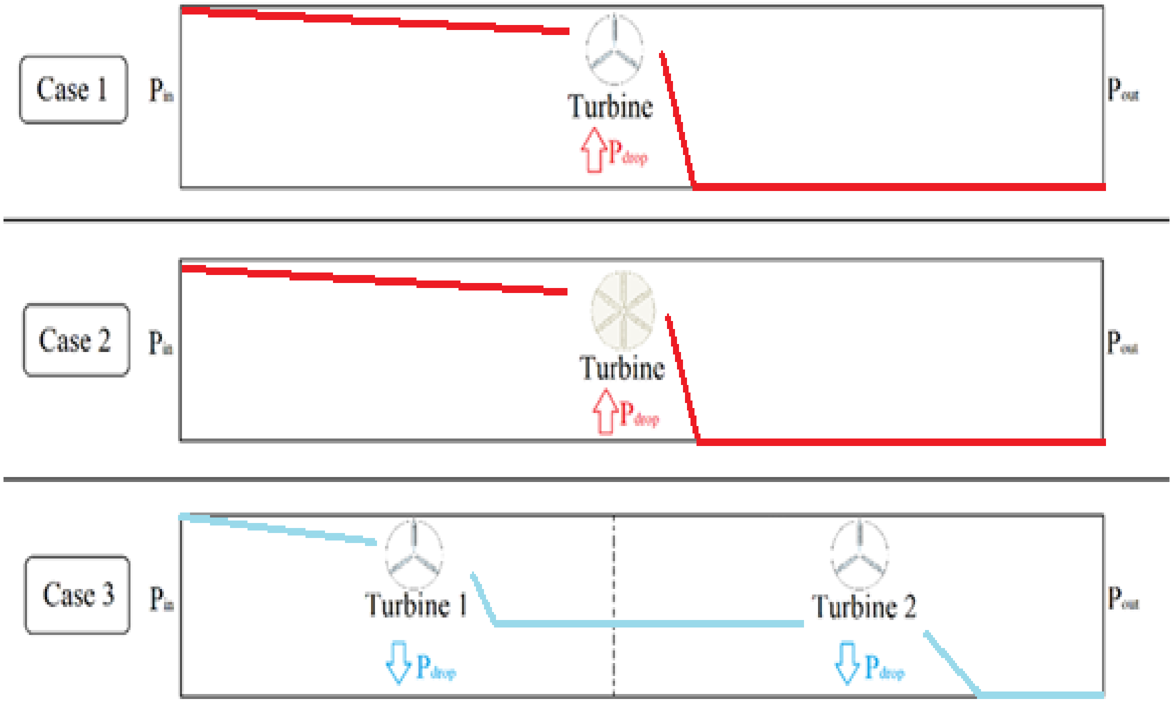

Figure 2. Illustration of 3 cases

While the performance coefficient and pressure loads are important metrics for evaluating a turbine system, they alone do not provide a complete understanding of its cost-effectiveness and power generation. It should be noted that a turbine with high power coefficient may not necessarily produce the required amount of energy output. Therefore, in addition to these metrics, it is essential to consider the generated power output figures as a measure of the actual amount of energy produced by the system per unit of time.

1.5. Research Objectives

This work aims to simulate and access an RDT in generating power for a flow in a pipe. It can be done both in numerical and experimental ways. Thus, we have created a numerical simulation in ANSYS® Fluent platform to assess the generation of kinetic to mechanical (electrical) energy in water flow. Therefore, our objective is obtained in several steps, which are as follows:

a) Develop accurate numerical simulation
b) Evaluate the results and draw a conclusion
c) Identify key design factors affecting the performance

d) Reduce pressure loads on the blades

Chapter 2 – Methodology

As specified, this work aims to simulate and study power generation of a rim-driven hydro turbine. Therefore, the following steps to achieve the objective are conducted:

1) Generate a mesh for a turbine blade. Initially, the OpenProp tool will be used for the design of the turbine blade
2) Development of numerical simulation
    - Setting computational domain & boundary conditions
    - Meshing
    - Solution method
    - Post-processing

ANSYS Fluent (Ansys® Fluent, release 19.1) was used to create the numerical model. It approximates the flow by solving mass and momentum equations. The problem is steady-state, and incompressible, and turbulence is modeled using the k-ω SST model.

The geometric model was first configured in OpenProp (Epps, 2016) and later created in ANSYS DesignModeler. The motivation for using the OpenProp software lies within the fact that it allows us to generate a preliminary model of a ducted turbine, whose data on blade cavitation, curves on performance, and given geometry will be used in the subsequent analysis in ANSYS Fluent.

2.1 OpenProp configuration

OpenProp is a software used for the design of water turbines and propellers. It is based on an m-code of MATLAB with a simple but powerful User Interface (UI). The software configures the required model to obtain the necessary data for further simulations. Moreover, it is possible to specify each geometric parameter and get the data needed for different types of marine turbines, including RDTs. It contains pre-prepared code with multiple input parameters to generate various curve designs.

2.2 Computational Domain and Boundary Conditions

As demonstrated in Fig. 4, the geometric model for further simulations will be set with a diameter of 24.0 cm and 270.0 cm in length. The length of the 3rd case will be equal to 300.0 cm due to presence of additional turbine. The computational domain is divided into three zones, with front and back zones having an equal length. The middle zone has a length of 30 cm that contains three blades of an RDT. Detailed information on the blades can be found in Appendix B. Further, we have neglected the duct modeling because this is considered as a pipe wall located outside the computational domain.

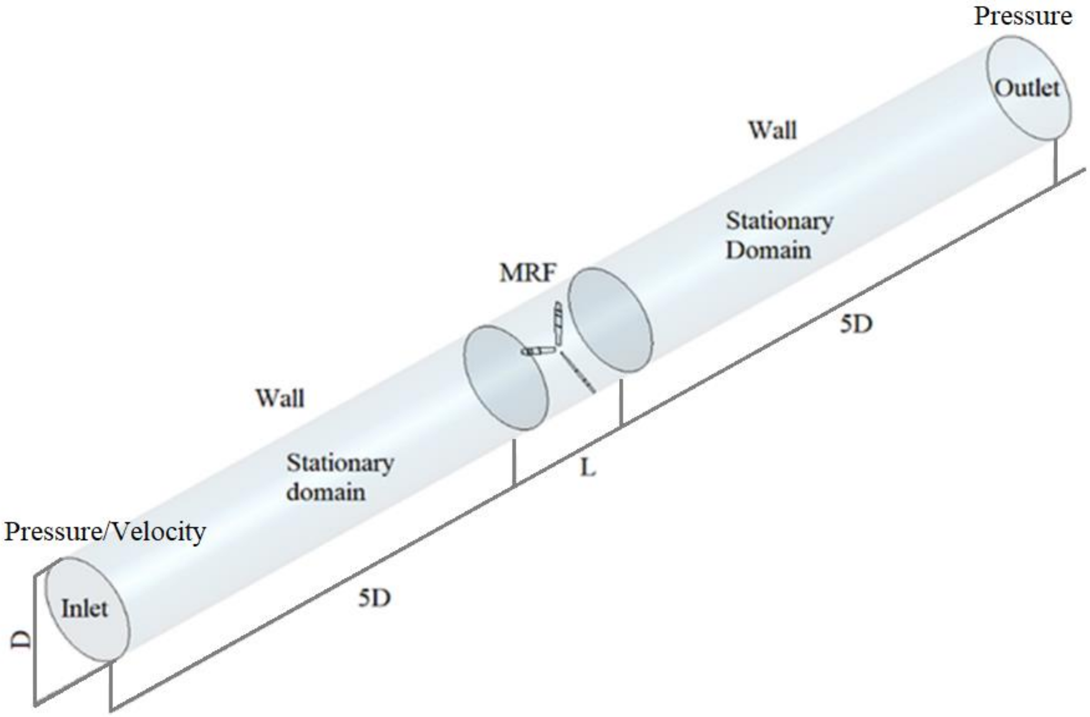

Figure 3. Geometric parameters and boundary conditions

The computational domain consists of three zones: "fluidzone1", "fluidzone2", and "fluidzone3". The front one contains the fluid coming from the inflow boundary, whereas fluidzone2 includes the fluid surrounding the blades. The "fluidzone3" is connected to the outflow boundary. The flow of water moves stream-wise in the positive y direction, while x and z coordinates represent horizontal and vertical axes. The computational domain is bounded by wall boundary conditions to simulate the flow in a pipe. Lastly, the outer and inner walls of "fluidzone2" (MRF zone) are connected as interfaces with the "fluidzone1" and "fluidzone3". The origin is located at the center of the MRF zone. To avoid unnecessary fluctuations during the simulation, we placed the inlet and outlet at an equal distance of 5D from the blades.

The velocity and pressure were specified at "velocity/pressure inlet" and "pressure outlet", respectively, with outer boundaries being set as "walls" to prevent mass flow leakage and simulate physical reality. Moreover, the middle computational domain is called Moving Reference Frame (MRF) zone.

2.3 Mesh of the 3-bladed turbine

As revealed in Fig. 5, the geometric model was divided into unstructured mesh with an element size of 10 mm at the MRF zone. In contrast, the rest of the computational domain is divided into a mesh of 70 mm in size.

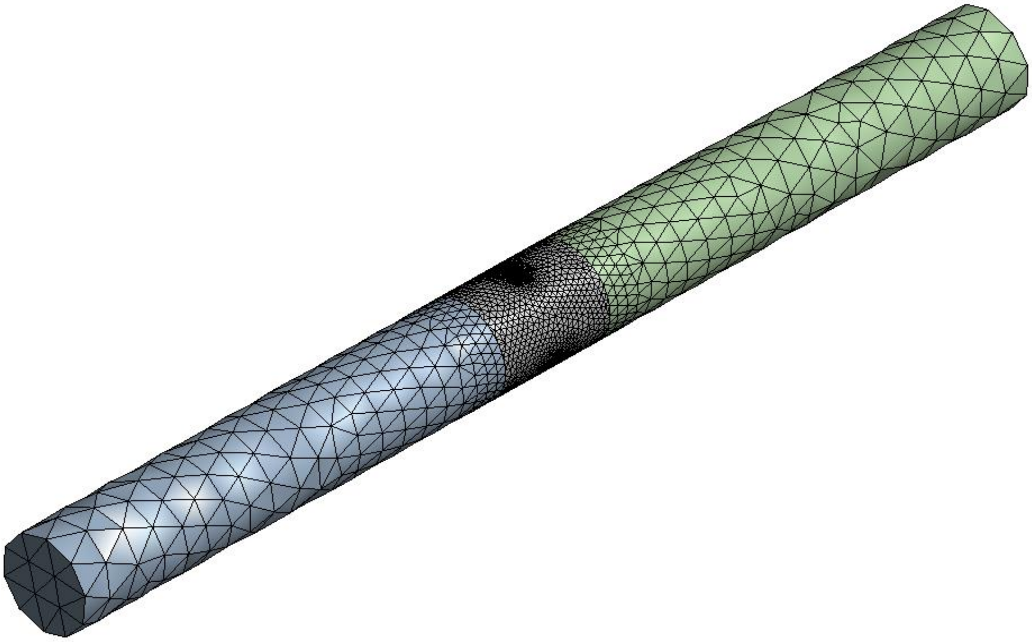

Figure 4. Mesh of 3-bladed turbine

As demonstrated in Fig. 6, the MRF zone was discretized with a denser mesh with a growth rate of 1.2, which is suitable for fluid flow problems. In addition, it is essential to check the accuracy of the solution by observing the pressure distribution on the blade surface; thus, geometric zones with high curvature were approximated with a high mesh concentration, which is the turbine blades in our case.

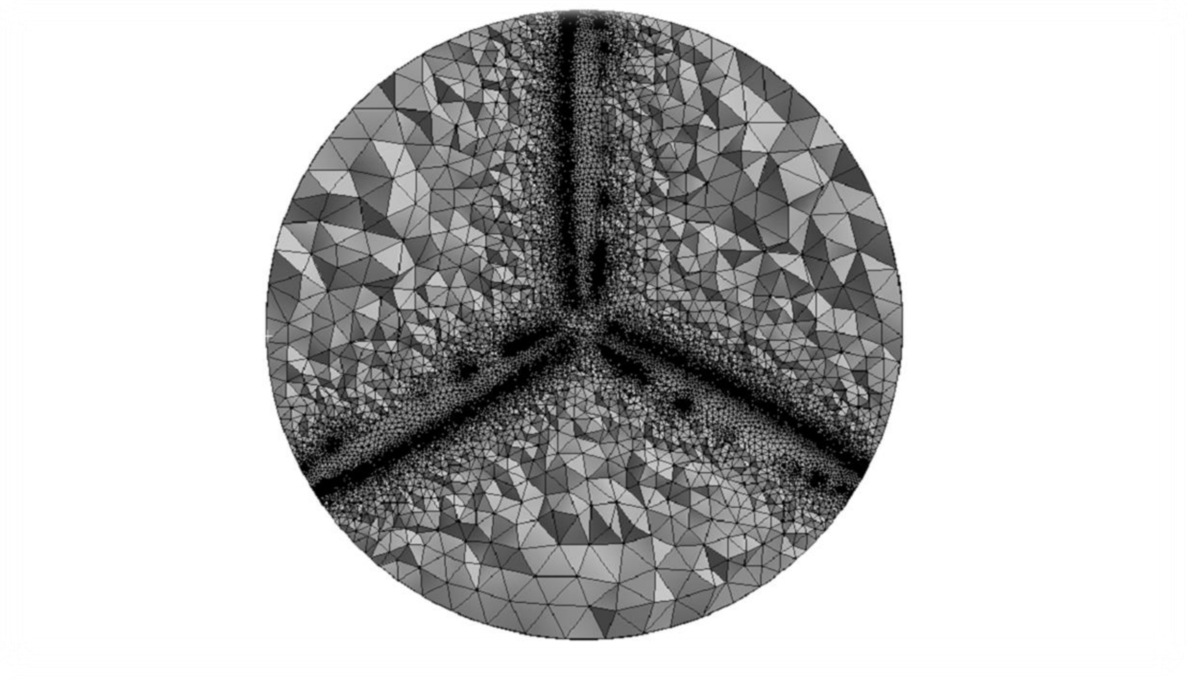

Figure 5. Section view of the 3-bladed turbine

2.4 Mesh of the 6-bladed Turbine

Similar to the 3-bladed case, the mesh for the 6-bladed turbine will consist of unstructured tetrahedral mesh with a 10 mm average element size in the MRF zone and 70 mm in the rest of the domain, as shown in Fig. 7.

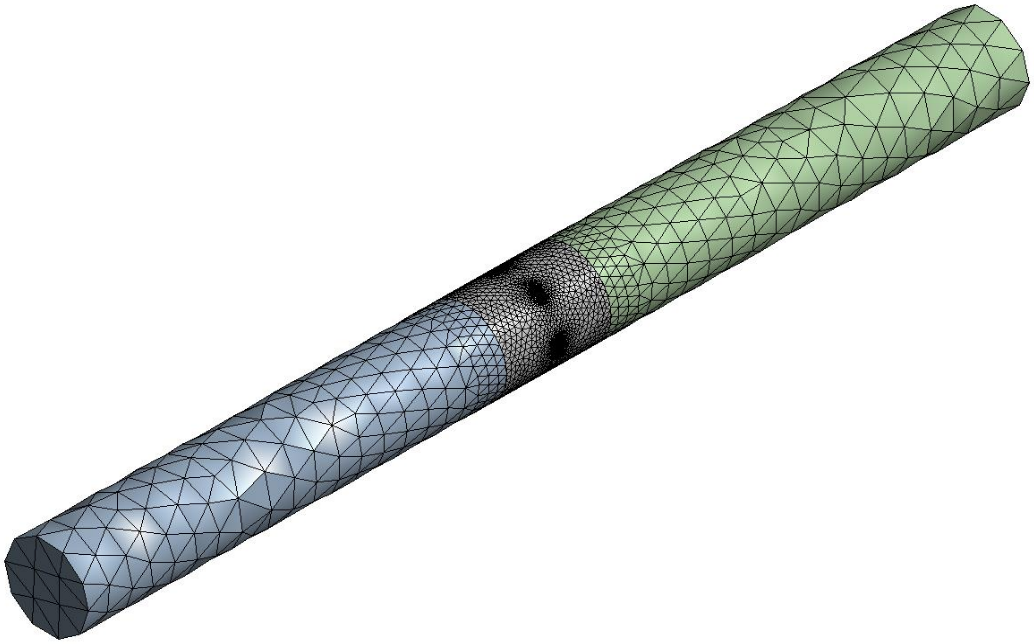

Figure 6. Mesh of the 6-bladed turbine

Identical to the 3-bladed cases, the MRF zone consists of dense mesh with high curvature capture. Note that additional blades increased the mesh count nearly twice, indicating high mesh concentration in the center, as demonstrated in Fig. 8.

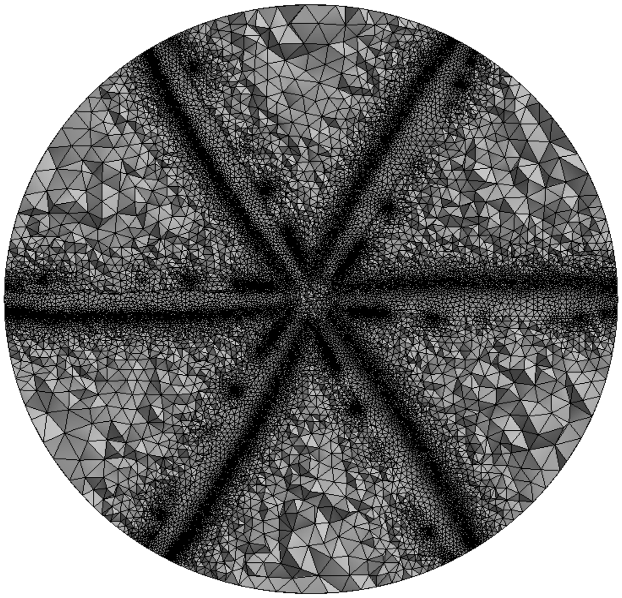

Figure 7. Section view of the 6-bladed turbine

2.5 Mesh of the 3-bladed series turbines

The meshing of the in-series turbines followed a similar approach with unstructured tetrahedral mesh with a high concentration in MRF zones. However, in the case of 3-bladed in-series turbines, it was decided to involve only two turbines for the initial study. Therefore, it included two MRF zones with counter-rotating blades to obtain a more accurate solution in steady-state simulation. The mesh for this case is demonstrated in Fig. 9.

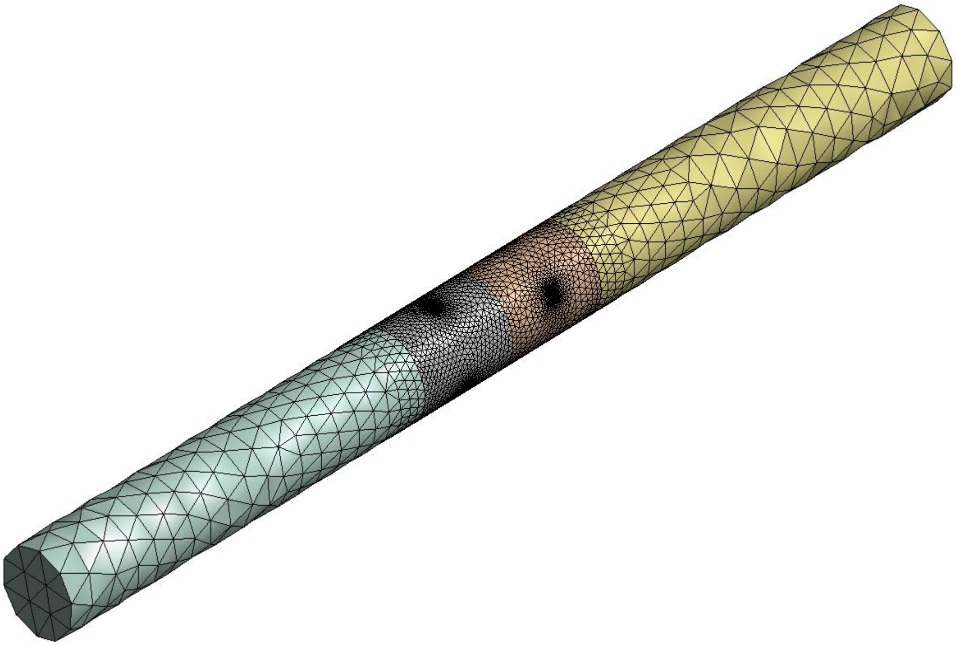

Figure 8. Mesh of the 3-bladed in-series two turbines

As it was mentioned, two turbines would be rotating in opposite directions. In addition, the front turbine is shifted to increase the accuracy of the MRF in a steady-state solution.

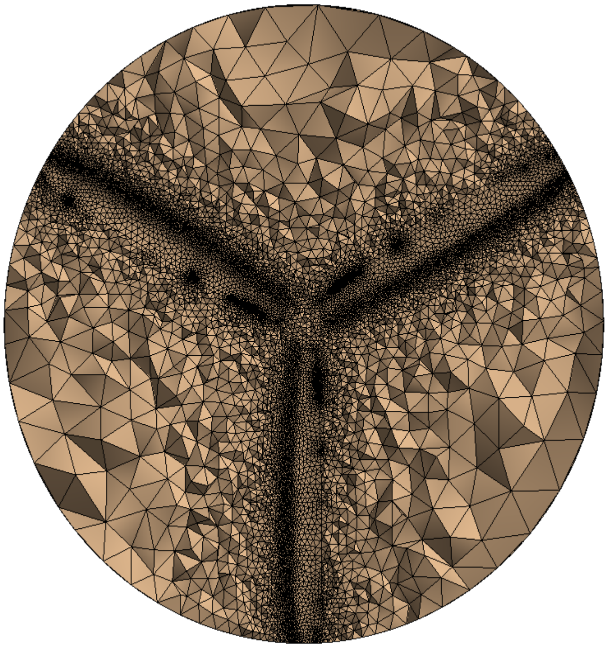

Figure 9. Section view of the front turbine

The back turbine has an identical mesh composition to the front turbine, as shown in Fig. 11.

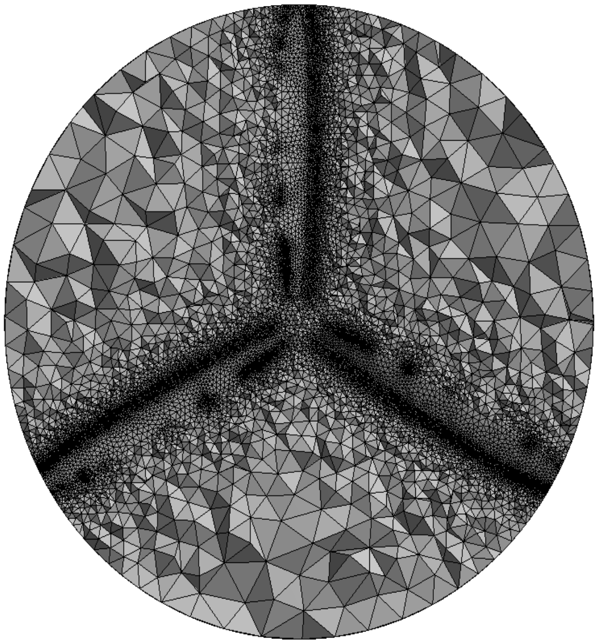

Figure 10. Section view of the back turbine

However, doubling the number of blades increases the mesh count substantially, affecting the memory and CPU demand and lowering the simulation's solution speed.

2.6 Solution Method

Since the case is a flow in a pipe, the pressure-velocity coupling solution method with the least-squared cell-based spatial discretization method is used. The detailed parameters are demonstrated in Table 1.

Table 1. Solution Methods

Solution method	Pressure-Velocity Coupling
Scheme	Coupled
Spatial Discretization	Least Square Cell-Based
Momentum	Second Order Upwind
Turbulent Kinetic Energy	Second Order Upwind
Specific Dissipation Rate	Second Order Upwind

To simulate the inlet, the $k-\omega$ SST turbulence model is used with a turbulence intensity of 10%.

All the residuals dropped below the criteria of 10E-3, which is not a direct indicator of solution convergence. Thus, it is essential to include additional variables and track their behavior during the iteration. In this case, I will include the torques at the blade's tip, whose steadiness during the solution will imply convergence.

2.7 Effect of simulating with velocity and pressure inlets

It is important to note that each hydro turbine operates in a range of TSR that generates a corresponding power coefficient characterized by the formulas (1) and (2).

$$\mathrm{TSR} = \frac{\omega \mathrm{R}}{V_0} \tag{1}$$

$$P = M\omega \tag{2}$$

$$C_p = \frac{\mathrm{P}}{0.5\rho S {V_0}^3} \tag{3}$$

Here, C_p represents the effectiveness of the whole turbine, measuring the portion of energy that is transformed from the kinetic energy of the water into power (3) compared to available energy in the surrounding fluid, and TSR shows the ratio between the velocity at a tip of a blade and free-stream velocity magnitude.

It is important to note that TSR is set up indirectly by defining inlet velocity or pressure in boundary conditions and varying the angular velocity at the MRF zone from a minimum to maximum value, generating the operating range using the formulas above. In summary, the methodology of generating different power coefficients for the range of TSR is as follows for velocity-inlet:

1. Defining constant inlet velocity
2. Specifying varying angular velocity at MRF
3. Generating inlet pressure data

The following power curve is generated with input parameters demonstrated in Table 2.

Table 2. Velocity-inlet input parameters

Inlet velocity, m/s	Minimum angular	Maximum angular	Fluid type	Density, kg/m³	Viscosity, kg/m*s

	velocity, rad/s	velocity, rad/s			
1.25	11.47	126.15	Water	998.2	0.001

The result of the velocity-inlet simulation is demonstrated in Fig. 12.

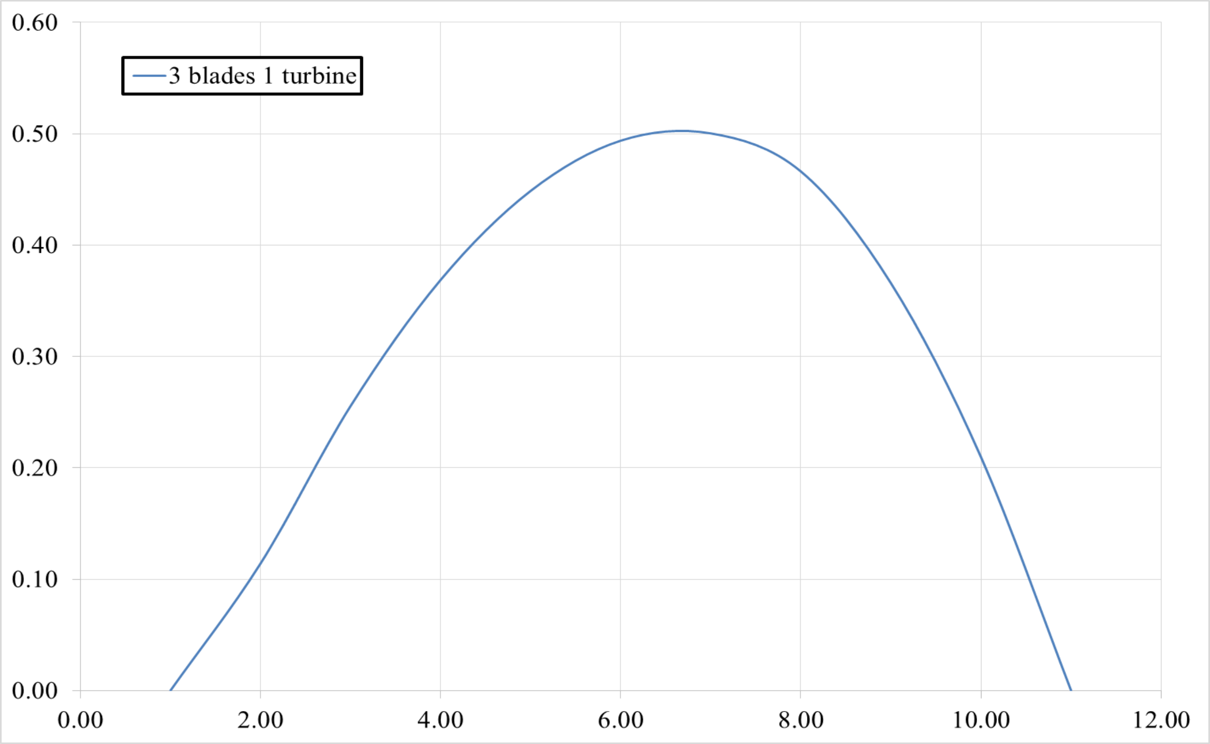

Figure 11. Velocity-inlet power curve

As the results demonstrate, the turbine operates in a given TSR range. However, the simulation was performed for constant free-stream velocity, which does not agree with physical reality, where inflow rates and speeds are erratic to a certain extent.

Further results are generated employing the pressure-inlet simulation as it closely approximates physical reality where the movement of the water is caused by pressure difference. The results for pressure-inlet simulation are obtained with the following steps:

1. Fixing angular velocity and specifying pressure-inlet using the data from velocity-inlet simulation on average pressure values at the inlet.
2. Calculating inlet velocity and TSR using formula (1)

3. Calculating power coefficient using formulas (2), (3).

Note that the methodologies mentioned above imply two ways of generating varying TSR, and first, fixing inlet values as in the example of velocity-inlet simulation and changing angular velocities. Second, defining constant angular velocity at MRF zone and changing the inlet values as in the example of pressure-inlet. Further results follow the second methodology with the input parameters specified in Table 3.

Table 3. Pressure-inlet input parameters

Angular velocity, rad/s	Minimum gauge total pressure at the inlet, Pa	Maximum gauge total pressure at the inlet, Pa	Fluid	Density, kg/m³	Viscosity, kg/m*s
80.28	975	21200	Water	998.2	0.001

2.8 Grid Independence Test

Discretization errors are a significant factor affecting the solution's accuracy. Therefore, The Grid Independence Test was conducted to derive how changes in spatial parameters affect the solution. As demonstrated in Table 4, three simulations were performed: coarse, medium, and fine elements.

Table 4. Results of Grid Independence Test

Mesh Density	Local Minimum Size, mm	Number of cells	C_p	% Change
Coarse	0.4	735366	0.62	
Medium	0.32	807412	0.65	4%
Fine	0.3	883408	0.67	3%

The results in Fig. 13 demonstrate that the medium and fine meshes have shown the most accurate results in calculating the power coefficiennt for different TSR values. This result is especially the case for higher angular speeds of the rotor, where the results are significantly affected for the coarse mesh for a slight change in angular velocity.

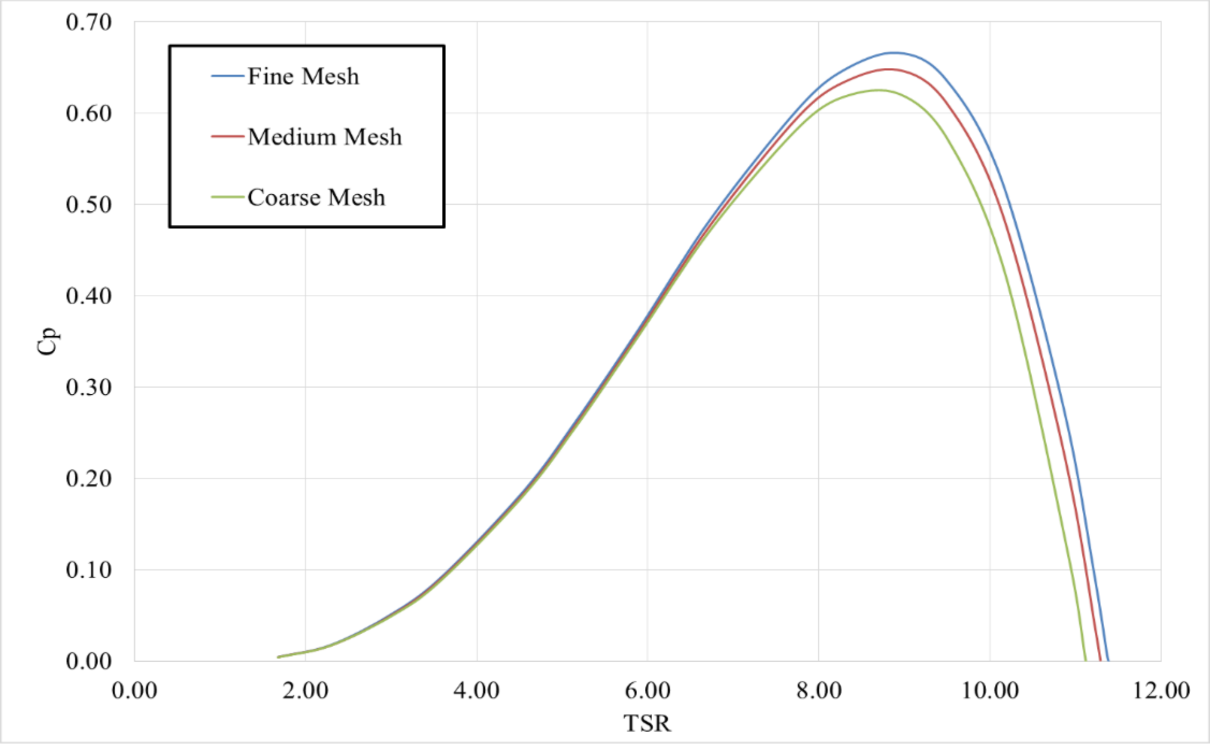

Figure 12. Comparison of different mesh

In essence, the grid independence was conducted by comparing the power coefficient in these cases, and the stop criterion was set to 5 %. As results demonstrate, the medium-density mesh was selected as an appropriate one for further calculations since consequent refinements do not significantly change results.

Chapter 3 – Results and Discussion

3.1 3 Bladed Single Turbine

The pressure on the front on the left side and back on the right side for the 3-bladed single turbine is demonstrated in Fig. 14. The simulation results were obtained for the inlet pressure condition of 1.5 kPa with 997 kg/m³ water density. The angular velocity of the MRF zone equals 80.275 rad/s.

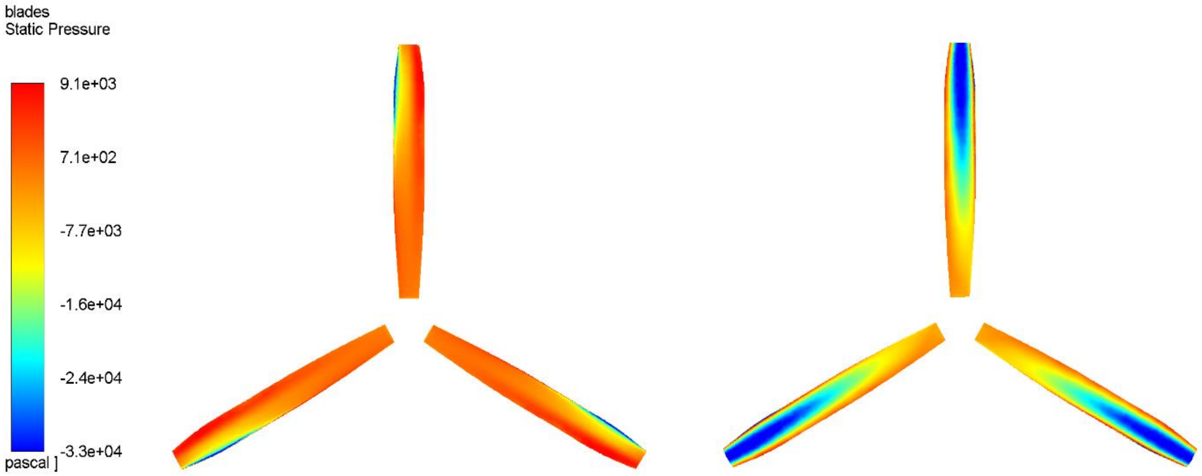

Figure 13. Pressure on blades

The turbine's suction side has negative pressures up to -33 kPa. The pressure side demonstrates that the leading edges of the blades are undergoing higher loads than the trailing edges, in agreement with reasonable expectations. The loads are exceptionally high at the tip of the blades indicating the most susceptible location to load regions.

The fluid particle flow is demonstrated in Fig. 15 for the same input conditions with 250 steps.

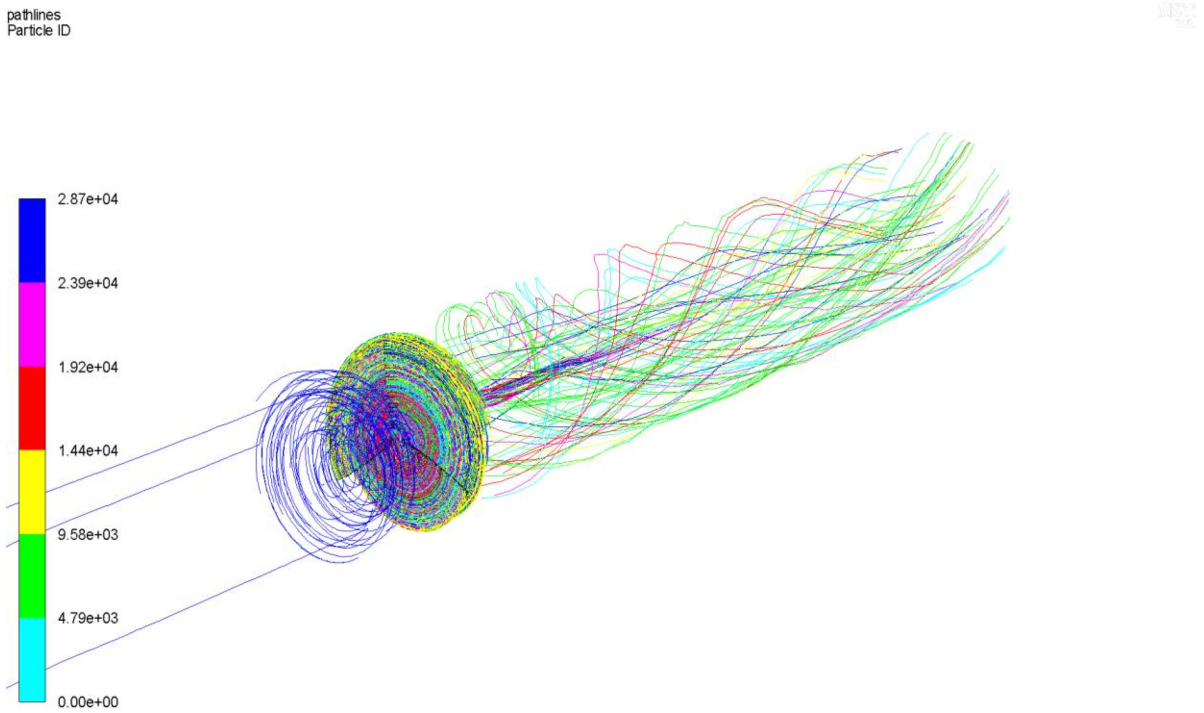

Figure 14. Water Flow around a RDT Single Turbine

Observing the water particle behavior near the turbine blade zone shows swirling flow behind the blades. A more detailed view of the swirling zone behind the blades is demonstrated in Fig. 16.

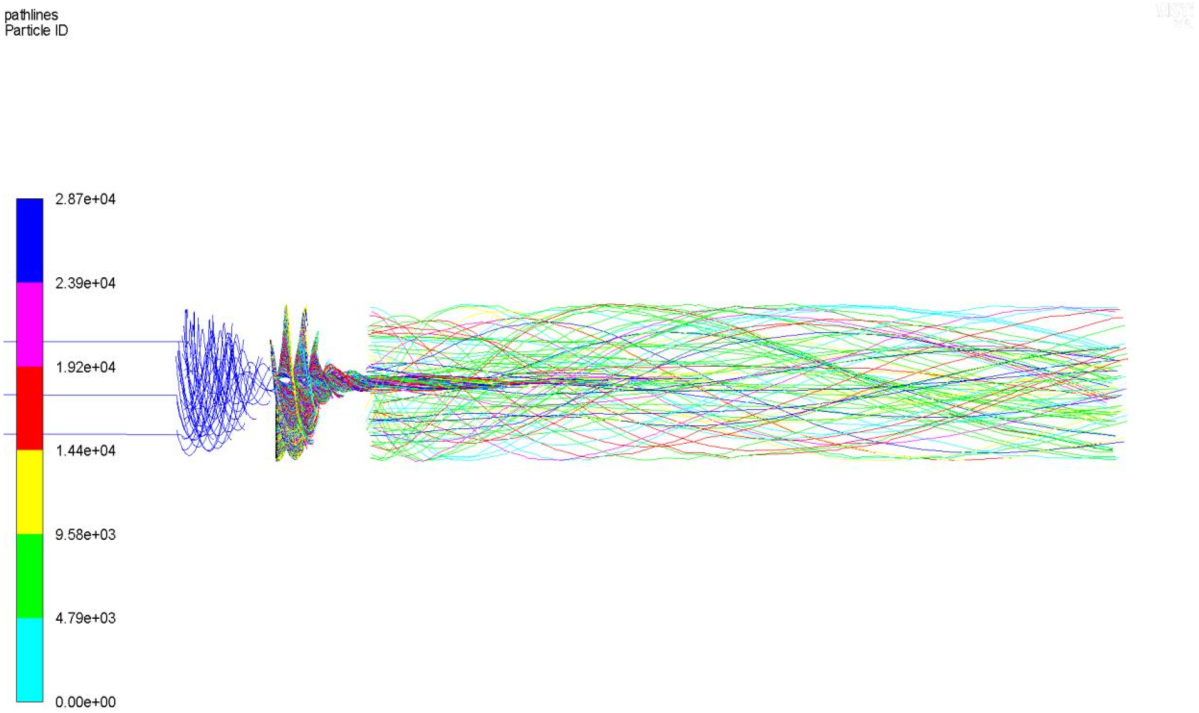

Figure 15. Side view of the particle flow

Figure 16 shows a strong presence of kinematic energy in the swirling water due to the blades' rotation, which can be harnessed by placing an additional turbine in it. Thus, placing a counter-rotating set of blades can capture the energy. Results in Fig. 17 show the power coefficient for the simulation.

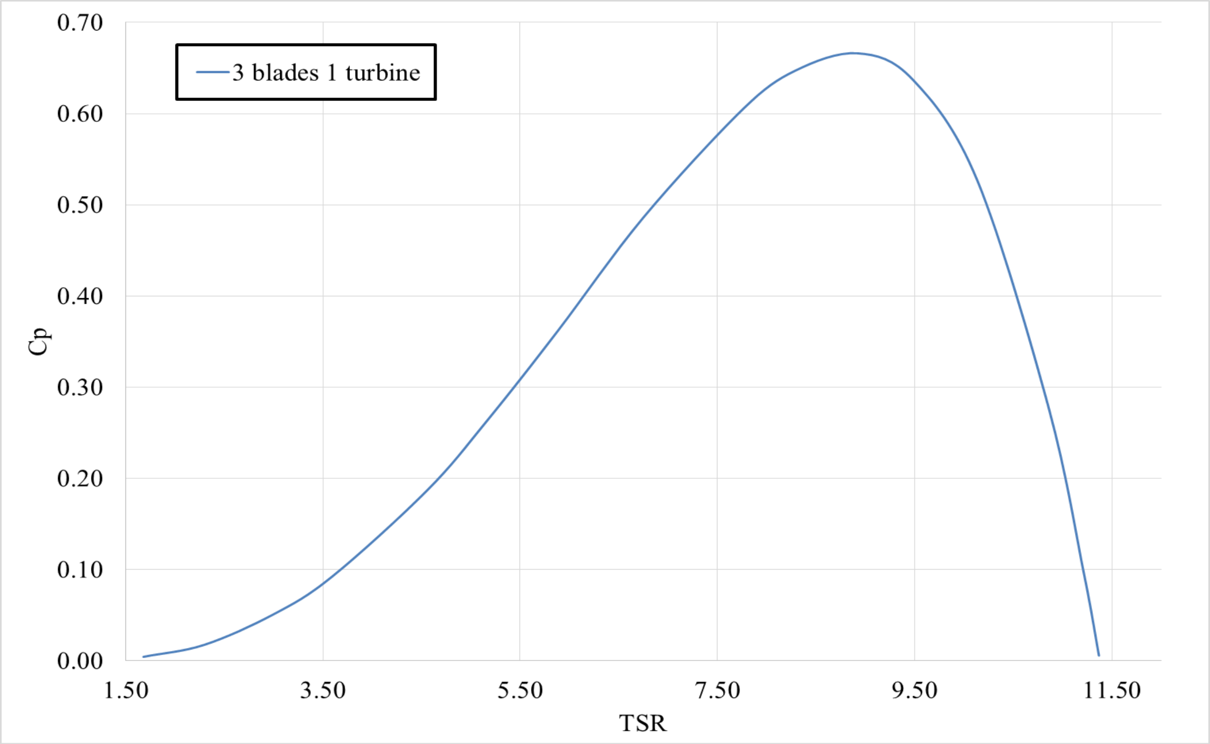

Figure 16. Power Curve of the 3-bladed single turbine

The simulation has demonstrated that the turbine reaches a maximum power coefficient of 0.67 at 1500 Pa pressure head or 0.98 m/s inlet velocity. The pressure drop across the turbine is shown in Fig. 18.

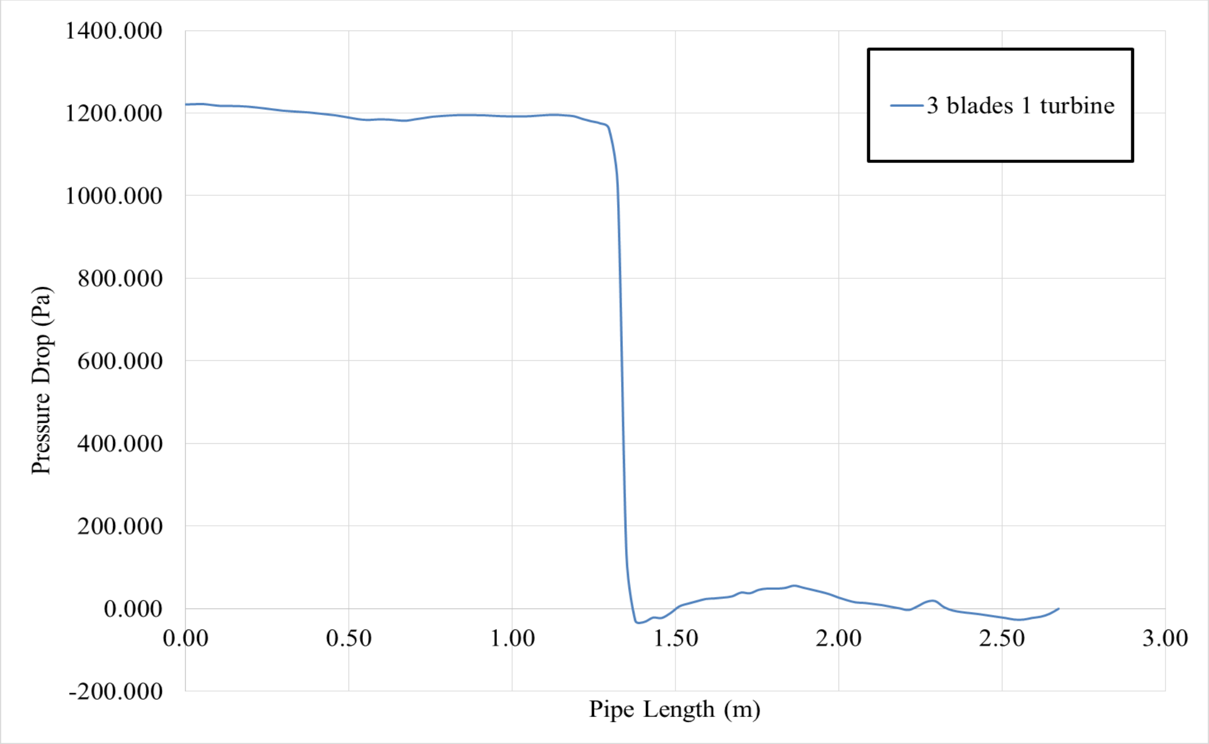

Figure 17. Pressure Drop for the 3-bladed single turbine

Figure 18 depicts the turbine undergoing a pressure drop from 1kPa that might be detrimental to its performance. Therefore, we will examine a scenario where two turbines are connected in a series arrangement to distribute the pressure loads as hypothesized. Subsequently, we will compare this setup with a 6-bladed configuration to determine if implementing a more costly turbine will yield a superior power coefficient, pressure loads, and power output compared to the alternative solution, where the number of blades is simply doubled at a lower cost.

3.2 6-Bladed Single Turbine

Similar to previous cases, the static pressure at the pressure and suction sides are demonstrated in Fig. 19. The results were obtained for 1.5 kPa pressure at the inlet with ~999 kg/m³ water density and clockwise angular velocity of 80.28 rad/s at MRF zone.

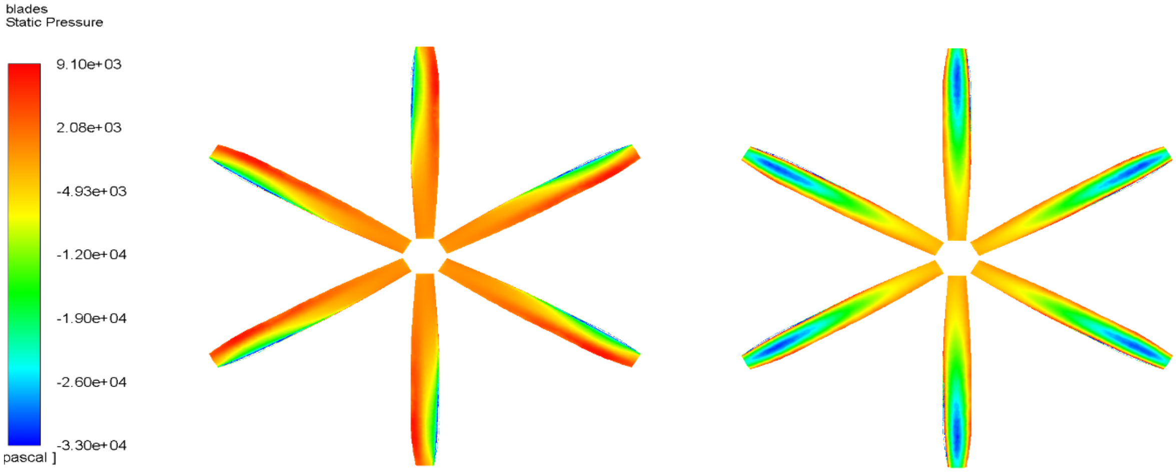

Figure 18. Pressure on blades

As shown in Fig. 19, the overall loads on the blades are much smaller compared to 3-bladed cases due to the distributed loads. Figure 20 shows the fluid flow around 6 blades after 250 steps.

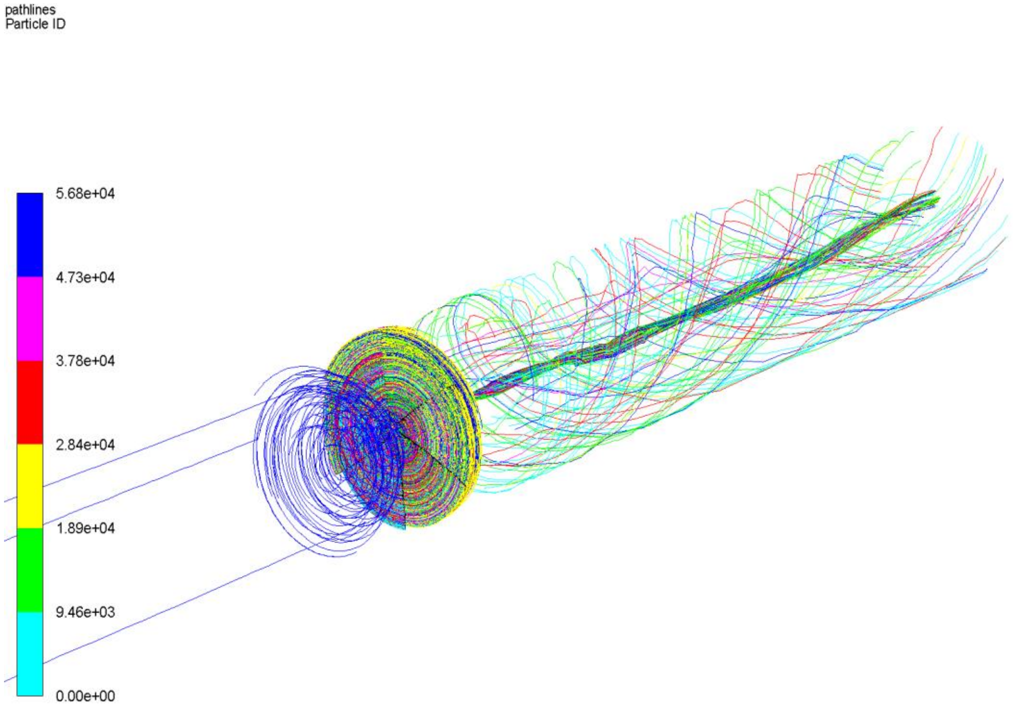

Figure 19. Pathlines with isometric view

The side view for an imaginary water particle path is shown in Fig. 21.

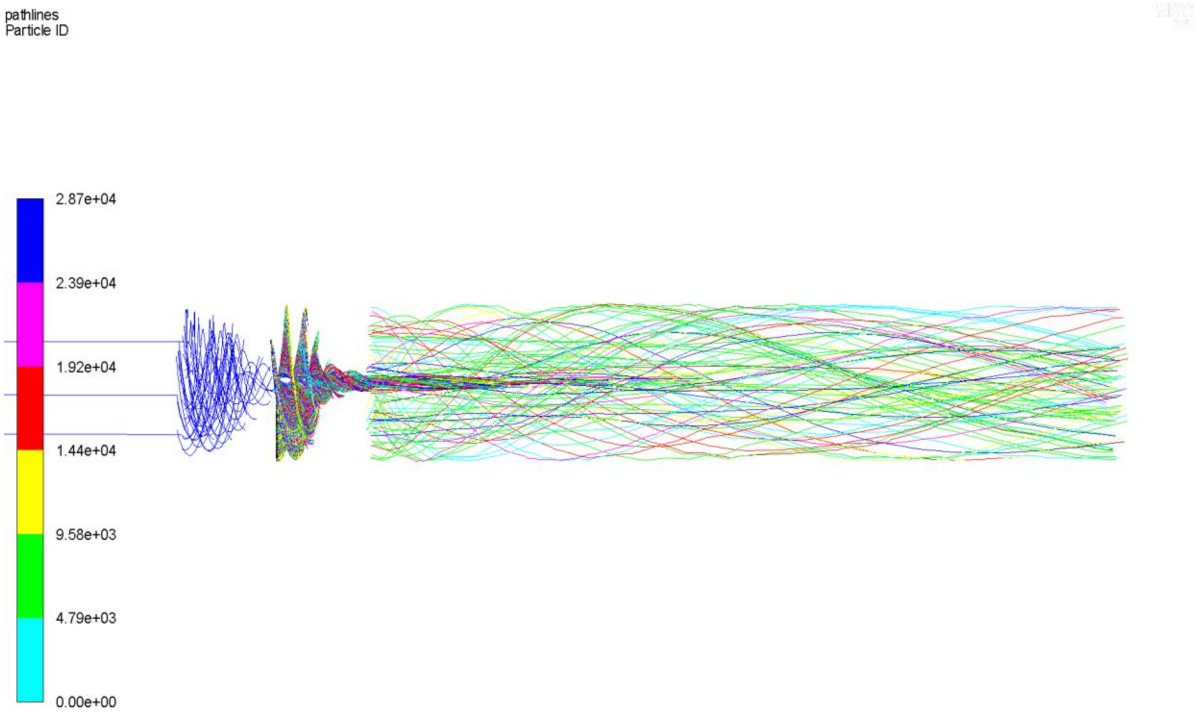

Figure 20. Pathlines with side view

Based on Fig. 21, it is evident that the swirling zone located at the back of the 6-bladed turbines has a significantly reduced size compared to the 3-bladed configuration. This difference can be attributed to the increased surface area obstructing the incoming fluid flow. The power coefficient of the 6-bladed turbine is described in Fig. 22.

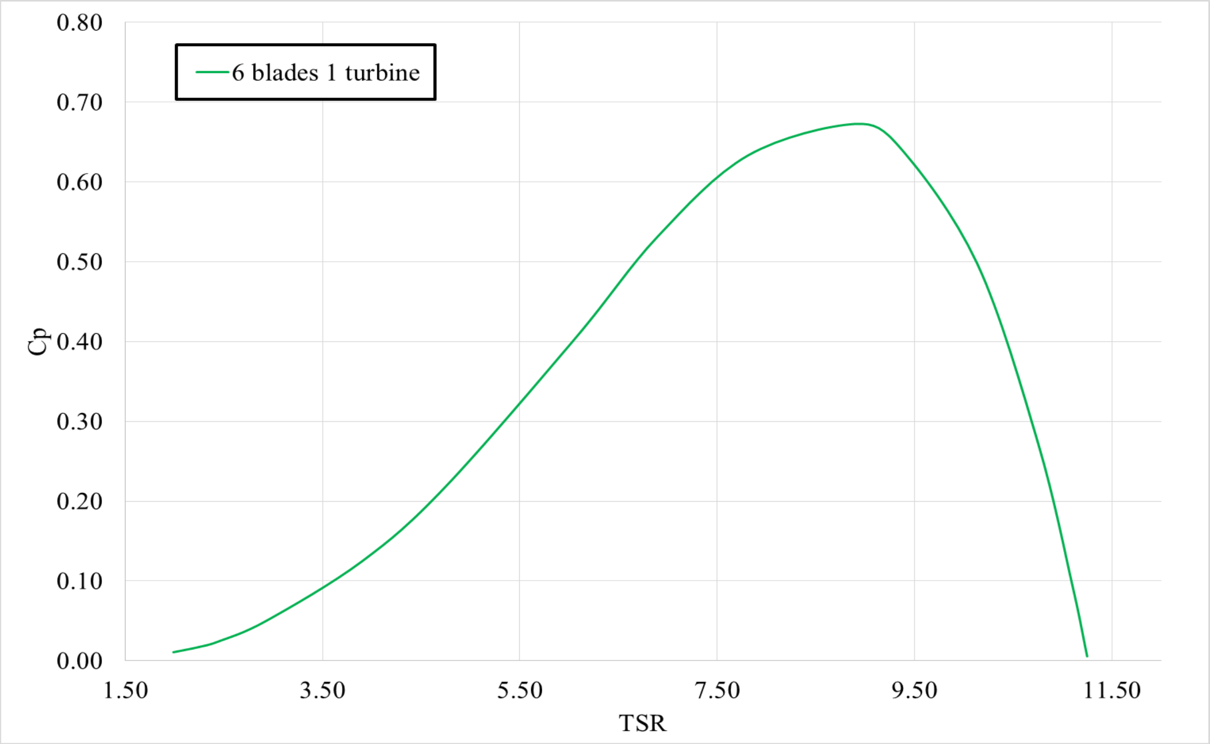

Figure 21. Power coefficient of the 6-bladed turbine

Figure 22 shows a peak power coefficient equal to 0.67 at 0.98 m/s flowing water velocity, similar to a single 3-bladed turbine case. The only difference is in pressure head values shown in Fig. 23.

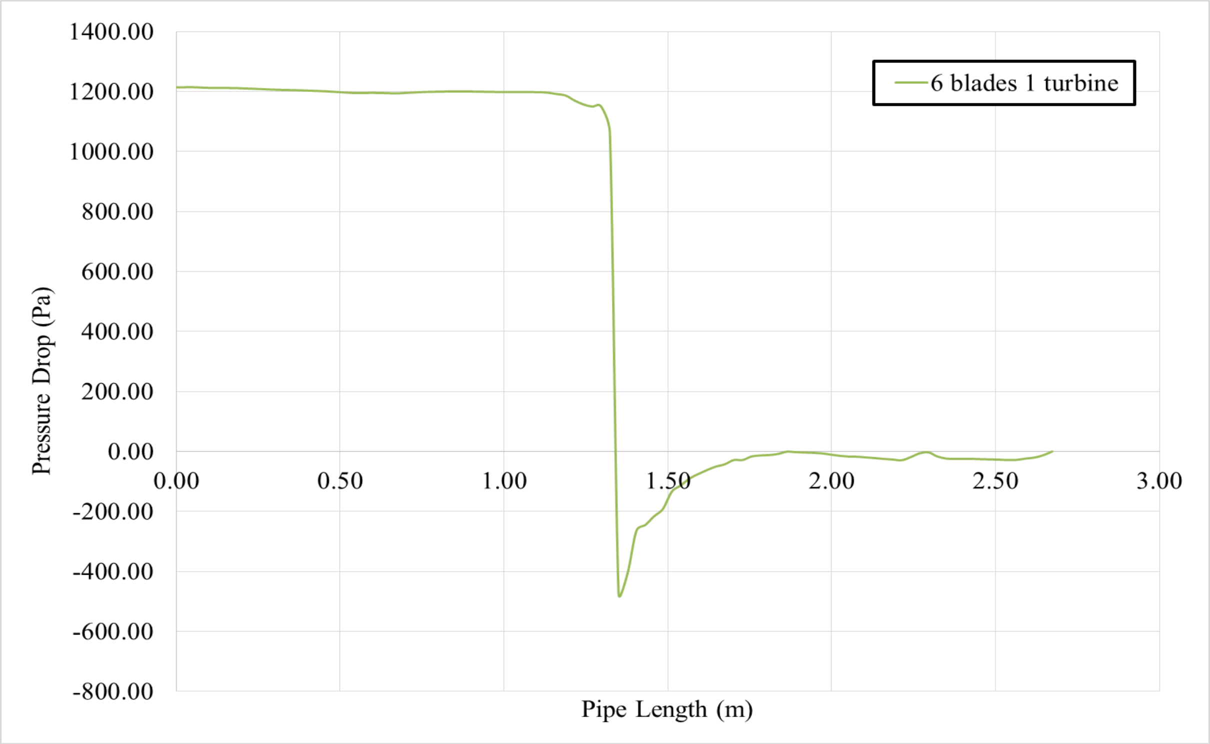

Figure 22. Pressure Drop of 6-bladed turbine

Similarly, the 6-bladed turbine is undergoing a pressure drop from 1.2 kPa, similar to the first case. However, as demonstrated in Fig. 19, this model is more resilient to large pressure loads due to the more significant number of blades.

3.3 Results Comparison: 3-bladed vs. 6-bladed turbine

Figure 24 compares the power curves for 3-bladed and 6-bladed single turbine simulations.

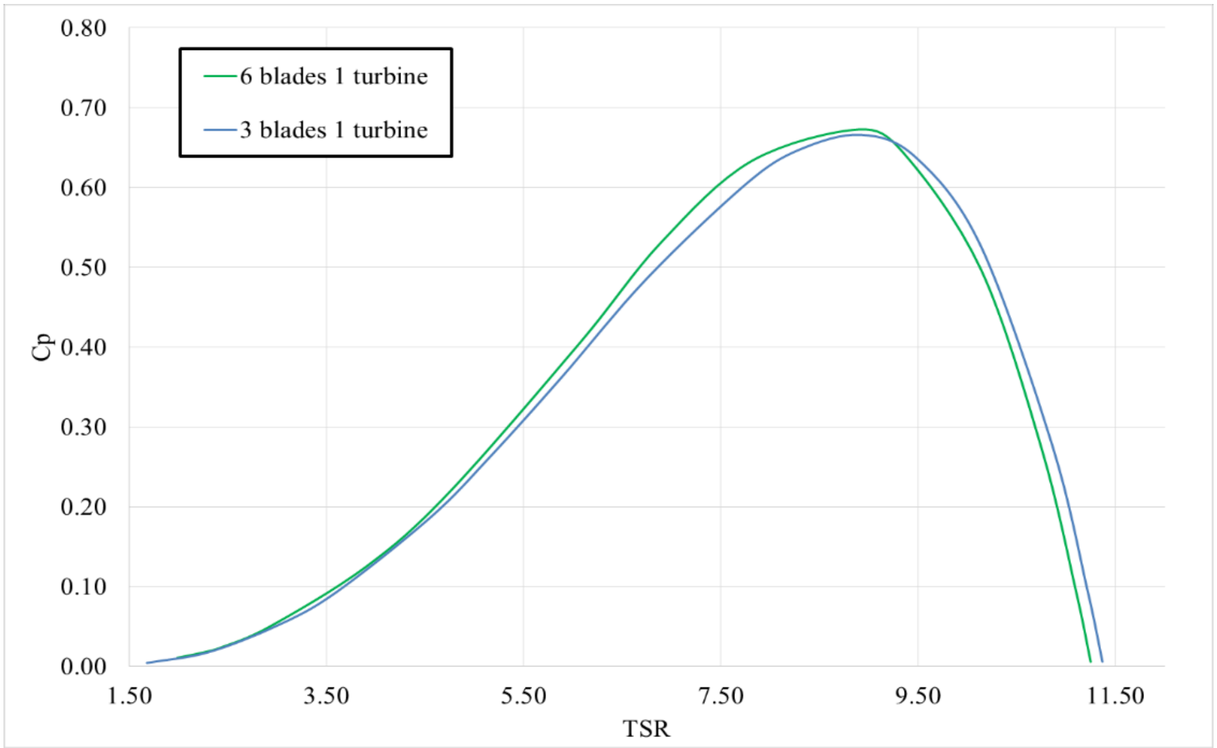

Figure 23. Comparison of Power Curves

The numerical results suggest that increasing the number of blades, as in the cases of a 6-bladed turbine compared to a 3-bladed turbine, does not significantly improve the power coefficient. Although it is slightly higher at low TSR values, this may be attributed to errors in the steady-state simulation. To conclude, the increase in the power coefficient achieved by increasing the number of blades in a single turbine is insufficient to justify the additional economic spending.

Figure 25 demonstrates how the blades of each turbine undergo pressure loads.

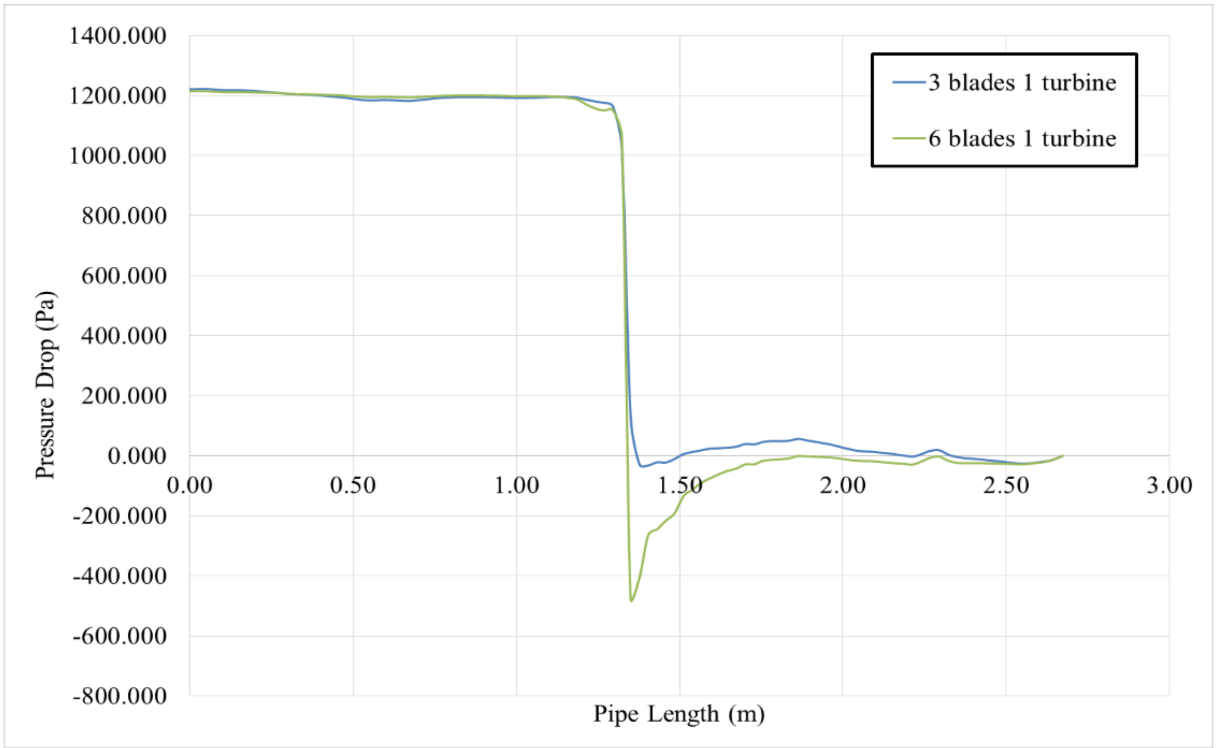

Figure 24. Pressure Load comparison

The pressure drop analysis across the simulated domain demonstrates that a single turbine with 6 blades is susceptible to experiencing elevated pressure drop values. The high-pressure drop can induce blade fatigue and damage over time, reducing lifespan compared to a single turbine with three blades. These findings suggest that a single turbine with 3 blades has superior power coefficient in the long term.

3.4 Counter Rotating Series 3-bladed Series Turbines

The results for the proposed counter-rotating in-series turbines are shown in Fig. 26.

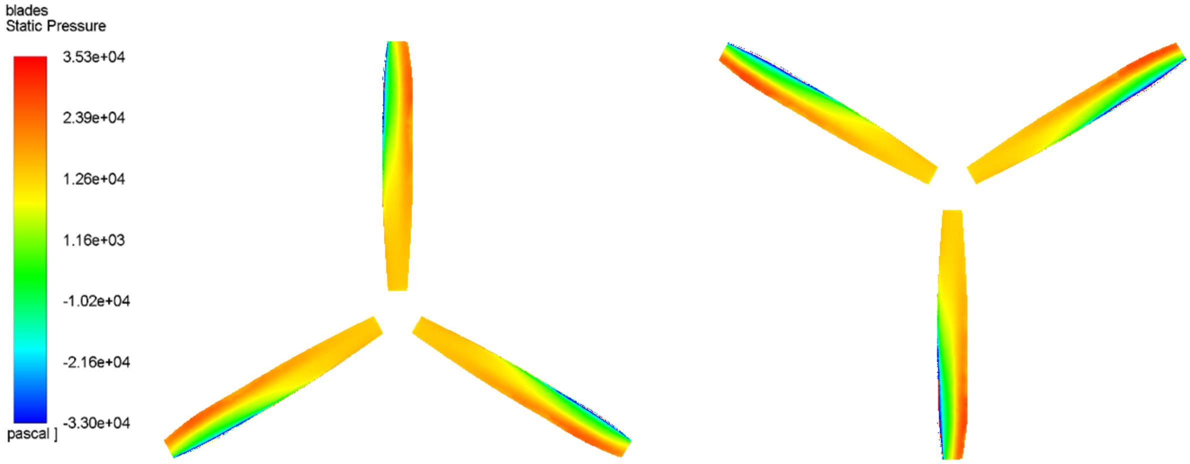

Figure 25. Isometric View of Pressure Side. 3-bladed two turbines

Observing Fig. 26, we can see the high-pressure loads on opposite sides of the leading edges, which comply with their rotating direction in Fig. 27.

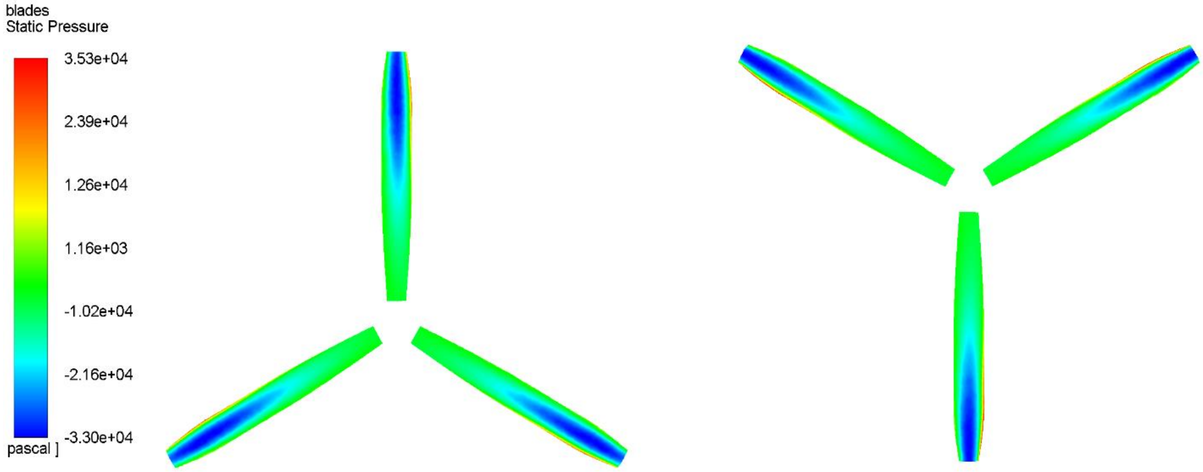

Figure 26. Suction Side of Front Turbine. 3-Bladed two Turbines

The pathlines with particles are shown in Fig. 28.

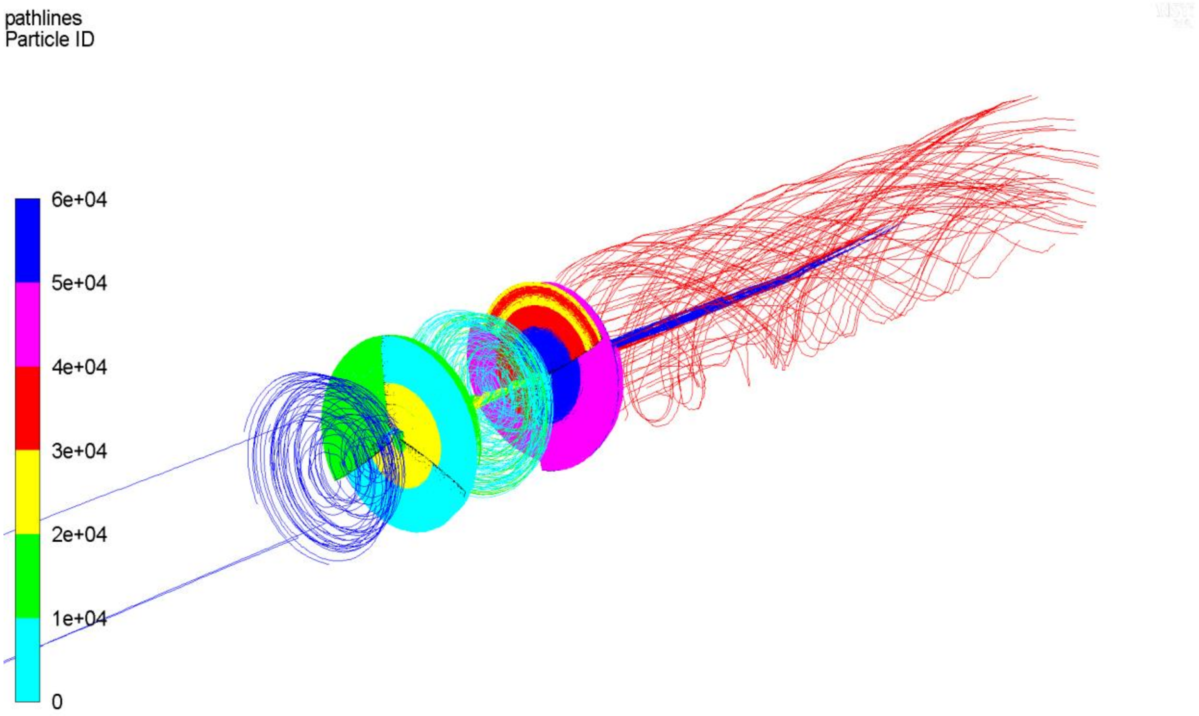

Figure 27. Pathlines around 3-bladed two turbines

Note the swirling flow behind each MRF zone, which is recovered by the back blades of the turbine. However, it might have a lower power coefficient due to less drag and reduced blade pressure. Therefore, it is necessary to calculate the produced amount of energy, power coefficient, and pressure drop to assess the viability of in-series turbines.

Figure 29 shows a side view of the pathlines.

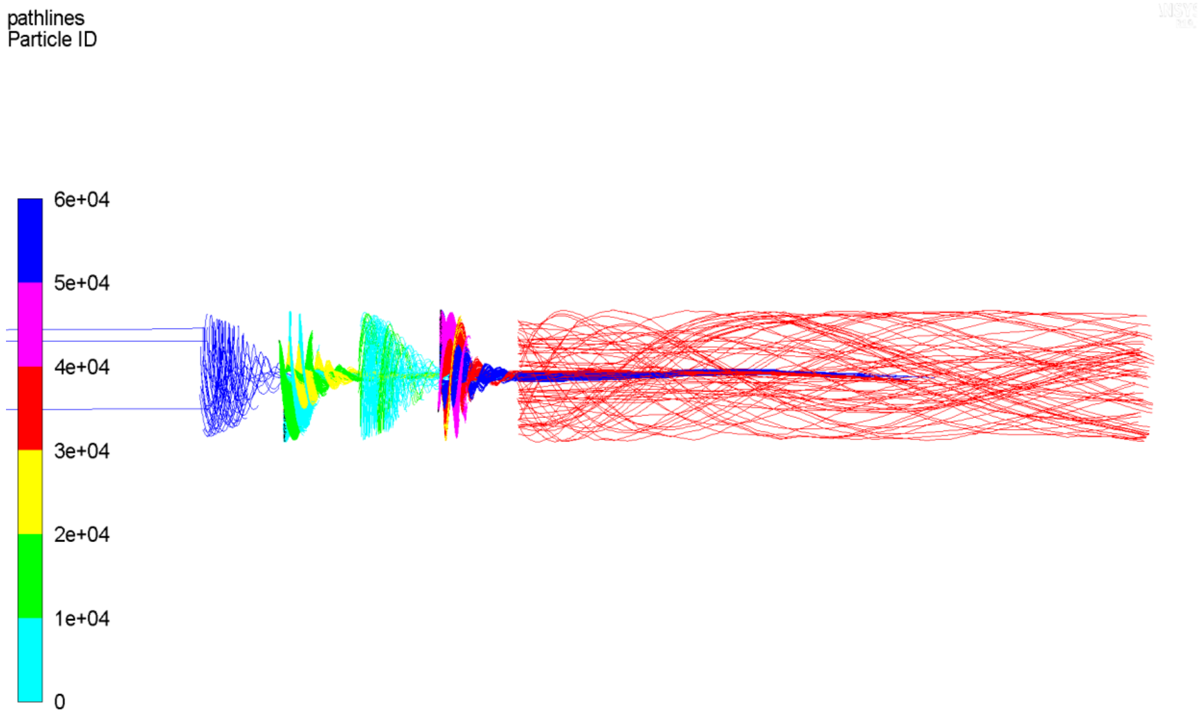

Figure 28. Side view of pathlines around 3-bladed two turbines

As shown in Fig. 29, the swirling zone denoted by red and green pathlines is relatively smaller than the front swirling zone in blue-cyan-colored particles, implying that a back turbine is recovering some of the energy from the front swirl. Theoretically, it is possible to calculate the maximum amount of viable in-series turbines based on Fig. 29, which is a subject for future studies. The power curve for the simulation is shown in Fig. 30.

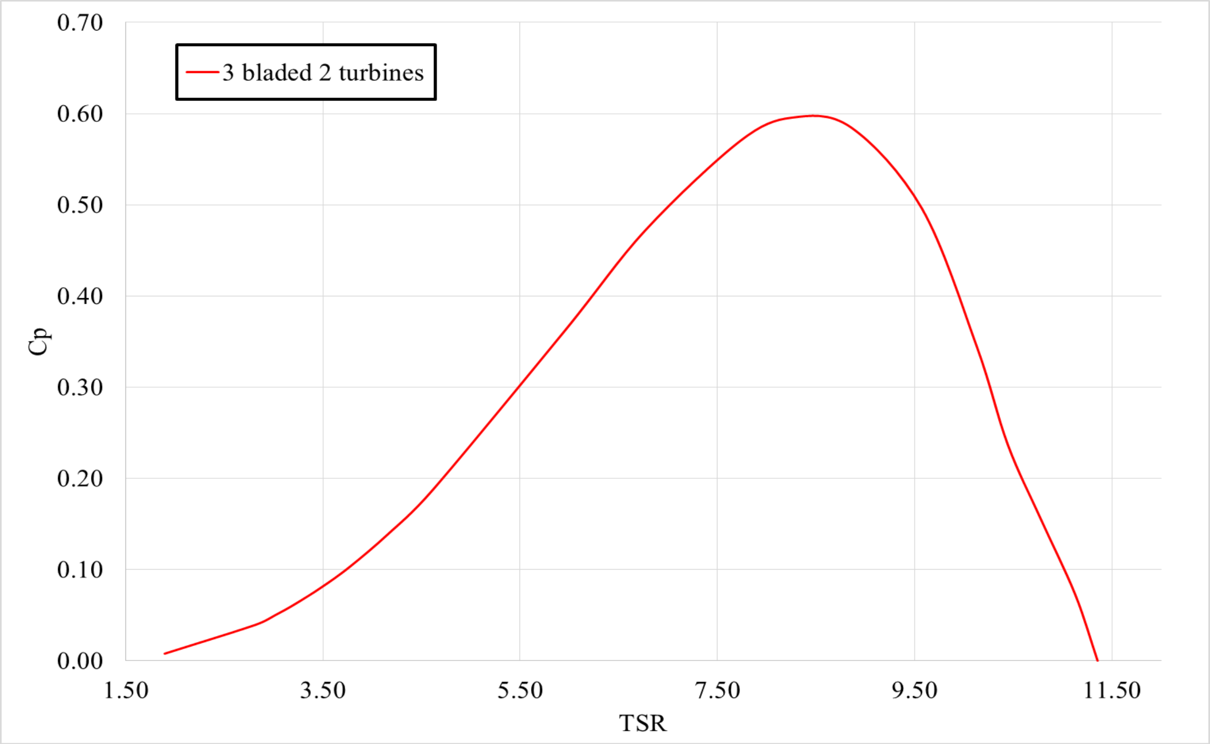

Figure 29. Power Curve. 3-bladed two turbines

The results took into account the power coefficient of both turbines. Interestingly, the peak value of 0.6 was reached at 2700 Pa head, or 1.06 m/s inlet speed, less than for a single 3-bladed turbine. Thus, two 3-bladed turbines generate lower power coefficients than single turbines in most scenarios. However, the main aim of in-series turbine placement was to achieve distributed loads to reduce the system's failure. Thus, the pressure loads are demonstrated in Fig. 30.

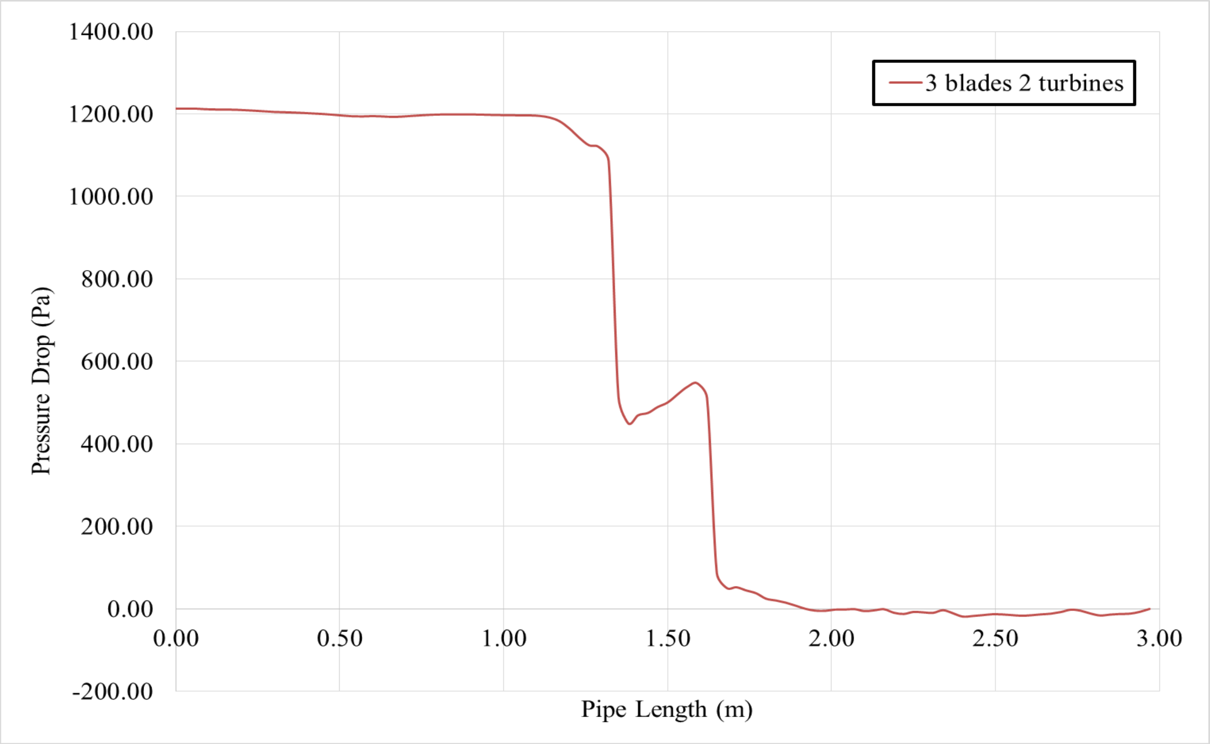

Figure 30. Pressure Drop. 3-bladed two turbines

Figure 31 depicts two pressure drops at points 1.25 m and 1.55 m, corresponding with the location of the turbines. For the first turbine, the pressure dropped from 1.2 kPa to 0.45 kPa. The second pressure drop corresponds to the 2nd turbine at the back. Hence, the first turbine undergoes a 750 kPa pressure drop, significantly lower than 1kPa, corresponding to a single hydro-turbine. Therefore, it is concluded that the in-series placement of the turbines reduces the pressure load on the turbines and reduces the chances of failure of the whole system.

3.5. Results Comparison for All Cases

Figure 32 demonstrates the power curves for all simulations mentioned above.

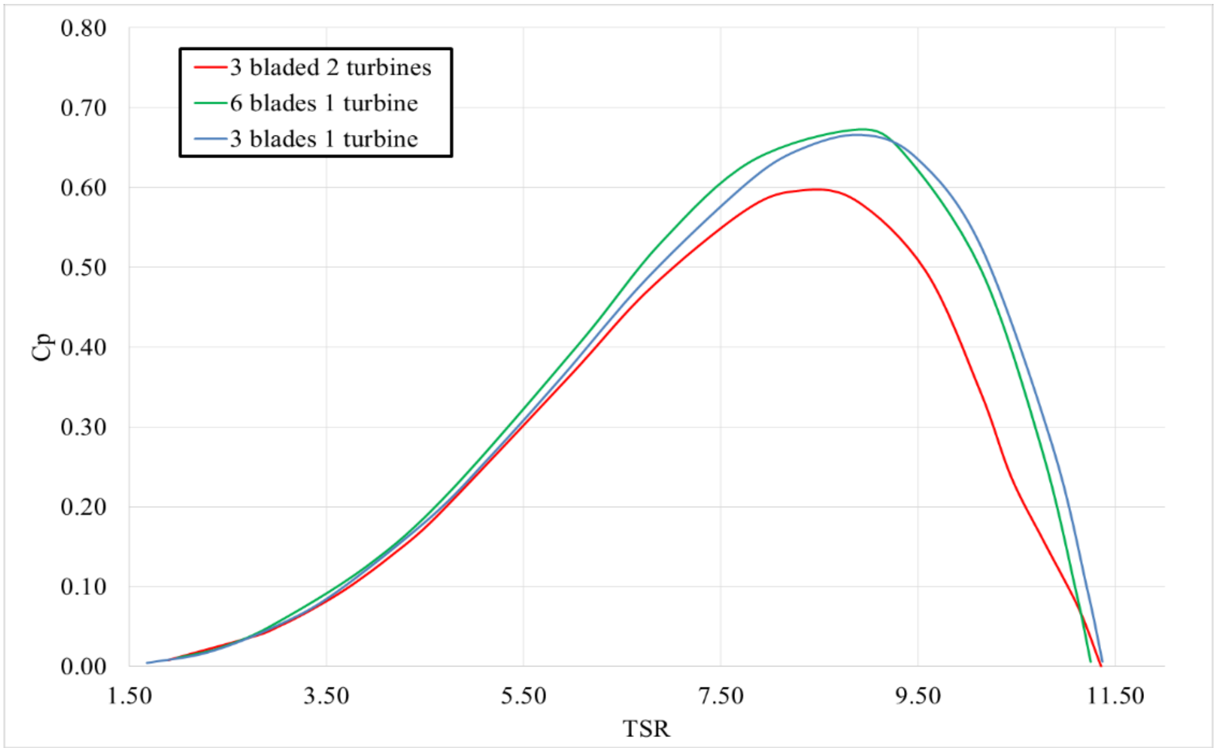

Figure 31. Power Curves: All Simulation Cases

The turbine outcomes were computed over the entire range of operating TSR and indicate that 6-bladed and 3-bladed single turbines demonstrate superior performance coefficients, with the former outperforming the latter. In contrast, in-series turbines show lower energy output, attaining 60% of the ambient kinetic energy at a peak TSR of 8.25, compared to the 3-bladed and 6-bladed single turbines, which achieve peak power coefficient of 0.6 at TSRs of 8.92 and 8.90, respectively.

However, as demonstrated in Fig. 33, the pressure loads tell a different story.

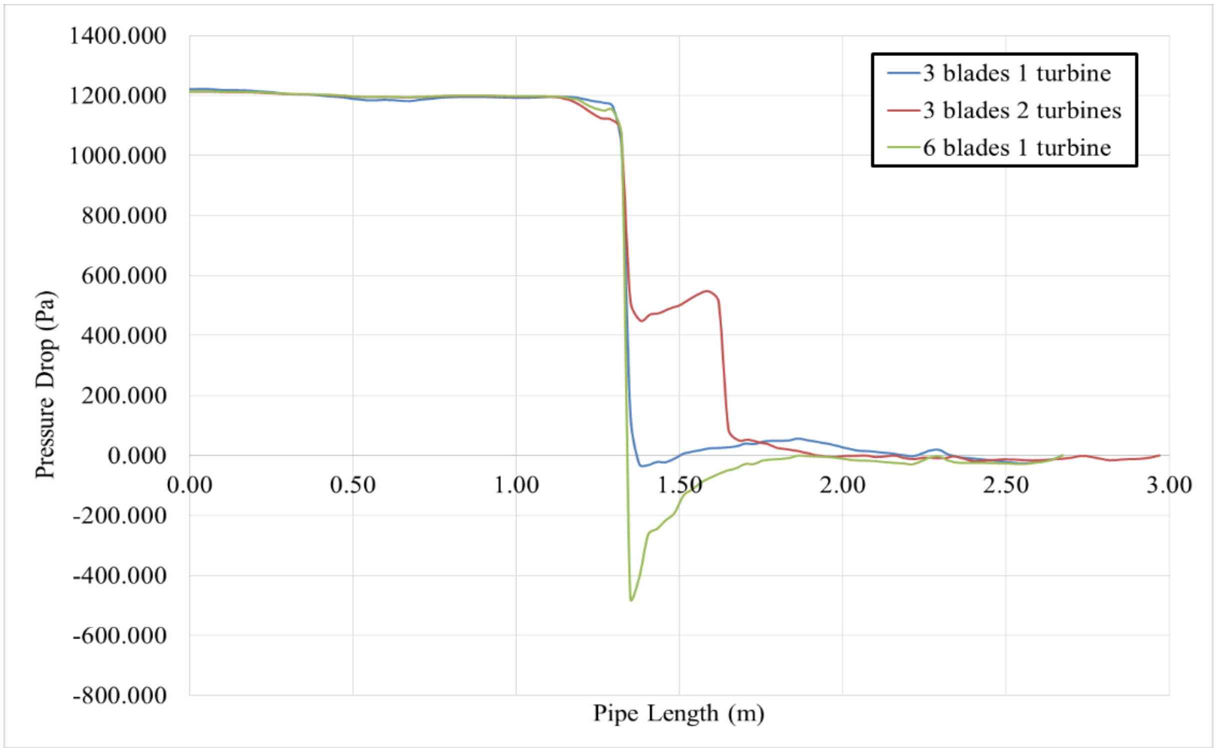

Figure 32. Pressure Loads Comparison

Based on Fig. 33, it can be stated that the 6-bladed single turbine has the highest pressure loads on the blade surface, which can have a detrimental effect on its operating lifespan. This is mainly attributed to its higher solidity, which results in a larger area subjected to pressure loads from the incoming water, leading to increased drag and generated energy, and reduced operating lifespan. In addition, it is suggested that 6-bladed turbines have a higher generated power but a lower lifespan compared to their 3-bladed counterparts; the latter exhibit comparatively lower pressure loads due to their lower solidity. The pressure loads are further reduced in the case of 3-bladed two turbines, as evidenced by the two pressure drops observed in the computational domain, corresponding to the location of the two turbines.

To conclude, our hypothesis regarding the placement of turbines in series reducing pressure on both turbines is supported by the results, with both the front and back turbine undergoing much lower pressure loads on their blade surfaces. Hence, in-series turbines have a longer operating lifespan. However, it is essential to consider the amount of generated power to draw meaningful conclusions regarding the viability of in-series turbines.

3.6 Generated Power Comparison

Figure 34 shows the amount of power generated for each case.

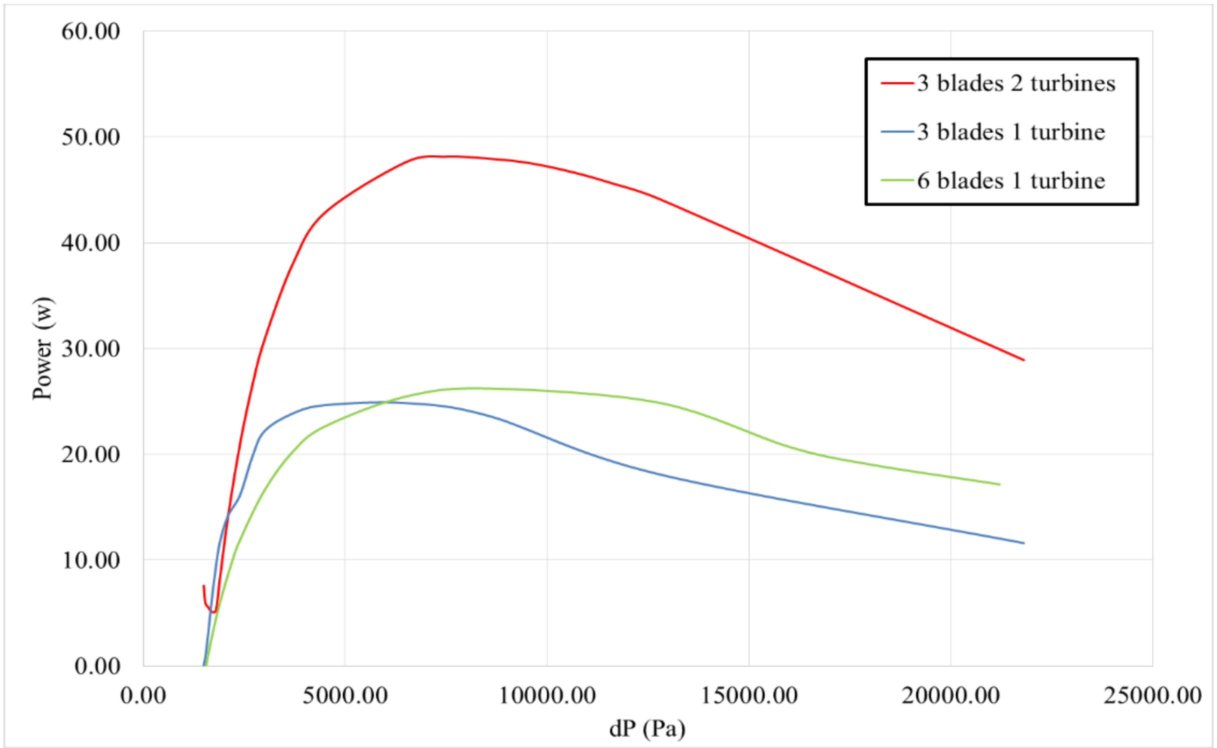

Figure 33. Power Generated in each case

Based on the results, 3-bladed in-series turbines present significant advantages in energy generation by recovering some of the flow, with the second turbine resulting in nearly twice the power output compared to the cases with single turbines. In contrast, 6-bladed and 3-bladed single turbines have comparable results, with the former being better by a small margin, which is explained by the fact that a 6-bladed turbine has twice the area to capture the kinetic energy of incoming water. The results show that introducing additional 3 blades to a single turbine system provides significant increase in produced energy at the free-stream velocity of 4.4 m/s. However, a 3-bladed turbine is a plausible choice offering higher power generation at lower inflow speeds due to the optimal operating TSR range. Nevertheless, turbines' in-series placement demonstrated convincing results in Power Output (PO) and pressure drop, indicating its positive impact on operating time and produced energy.

Conclusion

In summary, a range of RDT turbine designs was developed and analyzed on ANSYS Fluent, leading to several significant findings on turbine design and performance. First, the results showed that a 3-bladed hydro-turbine with a specific blade design could convert up to 67% of the kinetic energy of the surrounding water into mechanical (and subsequently electrical) energy. Second, the proposed in-series placement of the turbines decreased pressure loads on the blades by 62.5% for the front turbine. It was concluded that although the in-series turbines exhibit lower power coefficients than a 6-blade and a 3-blade single turbine, it produces a larger amount of power and has a longer operating lifespan and less fatigue due to distributed pressure loads on the blades. The results imply that an additional turbine can increase the power output of the overall system by a significant margin.

In contrast, the power output of a 6-bladed single turbine design was found to be similar to that of a 3-bladed single turbine, suggesting that adding more blades to a single turbine has a limited positive impact on its power output. These results provide valuable insights for designing and optimizing RDT turbines for future applications.

References

Abbas, A. I., Amano, R. S., Saravani, M. S., Qandil, M. D., & Sakamoto, T. (2019). Optimization of Kaplan hydroturbine at very low head with rim-driven generator. Journal of Energy Resources Technology, 141(11).

Djebarri, S., Charpentier, J. F., Scuiller, F., & Benbouzid, M. (2015). Design and performance analysis of double stator axial flux PM generator for rim driven marine current turbines. IEEE Journal of Oceanic Engineering, 41(1), 50-66.

Djebarri, S., Charpentier, J. F., Scuiller, F., & Benbouzid, M. (2014, November). Comparison of direct-drive PM generators for tidal turbines. In 2014 International Power Electronics and Application Conference and Exposition (pp. 474-479). IEEE

Djebarri, S., Charpentier, J. F., Scuiller, F., Benbouzid, M., & Guemard, S. (2012, May). Rough design of a double-stator axial flux permanent magnet generator for a rim-driven marine current turbine. In 2012 IEEE International Symposium on Industrial Electronics (pp. 1450-1455). IEEE.

Edwards, I. J., 1988. Electric motor rotor comprising a propeller, British Patent, GB2200802.

Epps, B. (2017). On the rotor lifting line wake model. Journal of Ship Production and Design, 33(01), 31-45.

Escaler, X., Egusquiza, E., Farhat, M., & Avellan, F. (2004). Cavitation erosion prediction in hydro turbines from onboard vibrations. In Proceedings of the 22nd IAHR Symposium on Hydraulic Machinery and Systems, Stockholm, Sweden (Vol. 1, No. CONF, pp. 1-10). International Association For Hydraulic Research.

Fialová, S., Pochyly, F., Kotek, M., & Jasikova, D. (2016). A Study of the Impact of Surface Hydrophobia on Hydraulic Loses and Velocity Profiles. In 19th International Seminar on Hydropower Plants.

Gieras, J. F., Wang, R. J., & Kamper, M. J. (2008). Axial flux permanent magnet brushless machines. Springer Science & Business Media.

Hannah Ritchie, Max Roser and Pablo Rosado (2022) - "Energy". Published online at OurWorldInData.org. Retrieved from: 'https://ourworldindata.org/energy' [Online Resource]

Hochhaus K. H. (2010). Rim-driven thruster. In Wikipedia. https://en.wikipedia.org/wiki/Rim-driven_thruster

Jiang, H., Ouyang, W., Sheng, C., Lan, J., & Bucknall, R. (2022). Numerical investigation on hydrodynamic performance of a novel shaftless rim-driven counter-rotating thruster considering gap fluid. Applied Ocean Research, 118, 102967.

Kim, J. H., & Sarlioglu, B. (2013, November). Preliminary design of axial flux permanent magnet machine for marine current turbine. In IECON 2013-39th Annual Conference of the IEEE Industrial Electronics Society (pp. 3066-3071). IEEE.

Kort, L., 1940. Elektrisch angertriebene schiffsschraube, German Patent : DE688114.

Mineshima, T., Onishi, K., & Miyagawa, K. (2019, March). Flow field and cavitation characteristics of hydrofoils coated with hydrophilic and hydrophobic polymers. In IOP Conference Series: Earth and Environmental Science (Vol. 240, No. 6, p. 062055). IOP Publishing.

Patella, R. F., Choffat, T., Reboud, J. L., & Archer, A. (2013). Mass loss simulation in cavitation erosion: Fatigue criterion approach. Wear, 300(1-2), 205-215.

Pierro, J. J., 1973. Gearless drive method and means. United States patent, US3708251.

Santoso, A., Arief, I. S., & Kurniawan, A. T. (2017). Performance analysis rim driven propeller as a propulsor using open water test. International Journal of Marine Engineering Innovation and Research, 2(1).

Schechtl, T., Hötzl, S., Rutschmann, P., & Knapp, W. (2017). Development of a Low Head Tidal Turbine. Part 2: Test Rig and Model Turbine Design. In EWTEC 2017. Proceedings of the 12th European Wave and Tidal Energy Conference (pp. 687-1).

Song, K., & Kang, Y. (2022). A Numerical Performance Analysis of a Rim-Driven Turbine in Real Flow Conditions. Journal of Marine Science and Engineering, 10(9), 1185.

Song, K., & Yang, B. (2021). A Comparative Study on the Hydrodynamic-Energy Loss Characteristics between a Ducted Turbine and a Shaftless Ducted Turbine. Journal of Marine Science and Engineering, 9(9), 930.

Song, K., Wang, W. Q., & Yan, Y. (2019). Numerical and experimental analysis of a diffuser-augmented micro-hydro turbine. Ocean Engineering, 171, 590-602.

Song, X., Weile S., & Haifeng W. (2017). Numerical and experimental study of the rim-driven marine current power system. Taiyangneng Xuebao/Acta Energiae Solaris Sinica, 38(1), 194-200.

Taylor, O. S., Repp, J. R., & Brown, D. W. (1989). U.S. Patent No. 4,831,297. Washington, DC: U.S. Patent and Trademark Office.

Yan, X., Liang, X., Ouyang, W., Liu, Z., Liu, B., & Lan, J. (2017). A review of progress and applications of ship shaft-less rim-driven thrusters. Ocean engineering, 144, 142-156.

Zhu, D., Xiao, R., & Liu, W. (2021). Influence of leading-edge cavitation on impeller blade axial force in the pump mode of reversible pump-turbine. Renewable Energy, 163, 939-949.

Appendices

APPENDIX A

The following Table 5 contain information for "NACA 65A010" airfoil.

Table 5. Airfoil information

Airfoile Type	Number of blade sections	Maximum chord/ hub diameter ratio	Maximum thickness/ chord ratio, mm	Meanline type, a
NACA 65A010	5	0.2173	0.1181	0.8

The coordinate file for modelling is shown shown in table 6.

Table 6. Coordinate file of blade sections

r/R=0.25	X, m	Y, m
	-0.00444	0.000525
	-0.00438	0.000504
	-0.00421	0.00044
	-0.00392	0.000337
	-0.00353	0.000198
	-0.00309	2.65E-05
	-0.00272	-0.00017
	-0.00233	-0.00039
	-0.0019	-0.0006
	-0.00143	-0.00079
	-0.00091	-0.00093
	-0.00031	-0.00101
	0.000333	-0.00104
	0.000991	-0.00104
	0.001648	-0.001
	0.002283	-0.00094
	0.00288	-0.00086
	0.003394	-0.00077
	0.003888	-0.00066
	0.004434	-0.00053
	0.004434	-0.00053
	0.004885	-0.00037

	0.005075	-0.00017
	0.005068	3.70E-05
	0.004938	0.000271
	0.004653	0.000506
	0.004219	0.000728
	0.003643	0.000927
	0.002938	0.00109
	0.002113	0.0012
	0.001181	0.001239
	0.000189	0.001212
	-0.00081	0.001136
	-0.00176	0.001028
	-0.00264	0.000902
	-0.00328	0.000776
	-0.00378	0.000671
	-0.00413	0.000595
	-0.00436	0.00055
	-0.00444	0.000525
r/R=0.48	**X, m**	**Y, m**

	-0.00695	0.001474
	-0.00685	0.001433
	-0.00655	0.001313
	-0.00606	0.001126
	-0.00538	0.000877
	-0.00457	5.62E-04
	-0.00374	0.000153
	-0.00283	-0.00034
	-0.00186	-0.00085
	-0.00086	-1.33E-03
	0.000174	-1.71E-03
	0.001216	-0.00198
	0.00224	-0.00215
	0.003216	-0.00224
	0.00412	-0.00226
	0.004928	-0.00222
	0.00562	-0.00212
	0.006165	-0.002
	0.006592	-0.00179
	0.006953	-0.00149
	0.006953	-0.00149
	0.007146	-0.00104
	0.007056	-0.00049
	0.006735	1.01E-04
	0.006233	0.000756
	0.005546	0.001412
	0.004692	0.002032
	0.003694	0.002582
	0.002579	0.003032
	0.001374	0.00334
	0.000112	0.00346
	-0.00116	0.003402
	-0.0024	0.003209
	-0.00356	0.002918
	-0.00461	0.002549
	-0.00544	0.002183
	-0.00609	0.001881
	-0.00656	0.001665
	-0.00685	0.001537
	-0.00695	0.001474

r/R=0.69	**X, m**	**Y, m**
	-0.00552	0.00081
	-0.00544	0.000789
	-0.0052	0.00073
	-0.00481	0.000641
	-0.00427	0.000523
	-0.00363	0.000371
	-0.00294	0.000157
	-0.00219	-0.00012
	-0.00138	-0.00041
	-0.00055	-0.00069
	0.000292	-0.00092
	0.001135	-0.00108
	0.001955	-0.00118
	0.002728	-0.00124
	0.003437	-0.00127
	0.004062	-0.00125
	0.004588	-0.0012
	0.004994	-0.00113
	0.005295	-0.00101
	0.005522	-0.00082
	0.005522	-0.00082
	0.005611	-0.00052
	0.005489	-0.00016
	0.005194	0.00023
	0.004757	0.000657
	0.00418	0.00108
	0.003479	0.001475
	0.002673	0.00182
	0.001785	0.002095
	0.00084	0.002274
	-0.00014	0.002327
	-0.00111	0.002263
	-0.00205	0.002108
	-0.00293	0.001886
	-0.00373	0.001608
	-0.00436	0.001335
	-0.00486	0.00111
	-0.00522	0.000949
	-0.00545	0.000855
	-0.00552	0.00081

r/R=0.85	X, m	Y, m
	-0.0048	0.00057
	-0.00473	0.000561
	-0.00452	0.000538
	-0.00419	0.000507
	-0.00373	0.000467
	-0.00317	0.000413
	-0.00255	0.000316
	-0.00188	0.000168
	-0.00116	-2.1E-06
	-0.00041	-0.00017
	0.000342	-0.00032
	0.00109	-0.00044
	0.001812	-0.00054
	0.002489	-0.00061
	0.003103	-0.00067
	0.003638	-0.0007
	0.004081	-0.00072
	0.004417	-0.00072
	0.00465	-0.00067
	0.004798	-0.00057
	0.004798	-0.00057
	0.004824	-0.00039
	0.004686	-0.00015
	0.004407	0.000114
	0.004007	0.000404
	0.003492	0.000692
	0.002877	0.000962
	0.002177	0.0012
	0.001413	0.001392
	0.000605	0.001521
	-0.00022	0.00157
	-0.00105	0.001541
	-0.00184	0.00145
	-0.00258	0.00131
	-0.00324	0.001122
	-0.00379	0.000932
	-0.00422	0.000776
	-0.00454	0.000664
	-0.00473	0.000599
	-0.0048	0.00057

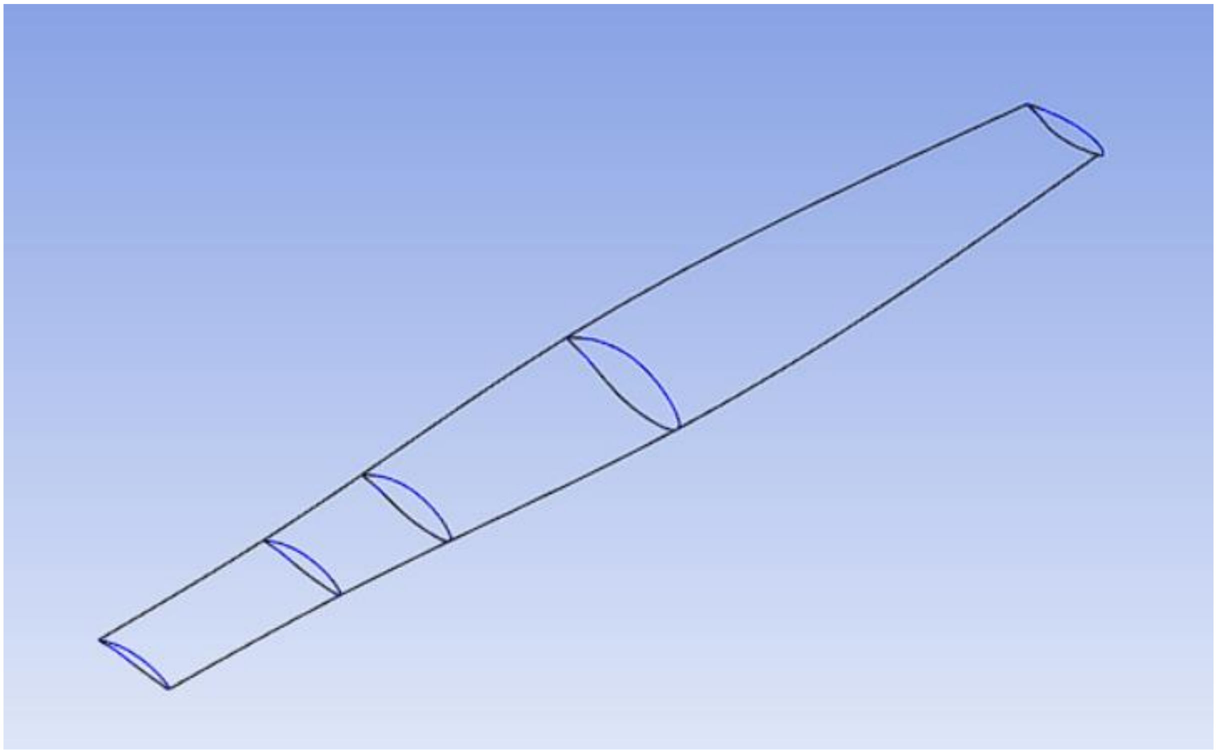

Figure 34. Model of Single Blade